QATAR UNIVERSITY

COLLEGE OF ARTS AND SCIENCES

ENHANCING THE THERMOELECTRIC PROPERTIES OF N-TYPE BISMUTH-TELLURIDE-BASED ALLOY USING GRAPHENE AS A NANOFILLER

BY

FARAH ELMAKATY

A Thesis Submitted to

the College of Arts and Sciences

in Partial Fulfillment of the Requirements for the degree of

Masters of Science in Material Science and Technology

June 2020

COMMITTEE PAGE

The members of the Committee approve the Thesis of
Farah Elmakaty defended on 11/05/2020.

Dr. Khaled Youssef
Thesis/Dissertation Supervisor

Dr. Ahmed Abdala
Committee Member

Dr. Ahmad Ayesh
Committee Member

Dr. Andre Mkhoyan
Committee Member

Approved:

Ibrahim AlKaabi, Dean, College of Arts and Sciences

ABSTRACT

ELMAKATY, FARAH, M., Masters : June : 2020, Material Science and Technology

Title: Enhancing the Thermoelectric Properties of N-type Bismuth-Telluride-Based Alloys Using Graphene As A Nanofiller

Supervisor of Thesis: Dr. Khaled Youssef

Bismuth telluride chalcogenides are the ideal thermoelectric materials used for near room temperature applications. However, the usage of these materials is relegated to a few applications as a result of the extremely low heat conversion efficiencies. In this study, graphene is used as a nanofiller to prepare n-type bismuth telluride nanocomposite of a composition $Bi_2Te_{2.7}Se_{0.3}$. The samples were prepared via a ball milling technique with different graphene concentrations and processing times. The results revealed that graphene addition during the last phase of milling improved the thermoelectric properties. However, these enhancements were limited to the lower graphene concentration of 0.05 wt.% only. Moreover, the figure-of-merit values of the optimum sample showed noticeable enhancements of 19%, reaching 0.5 at room temperature and 23 % at 160 ºC, reaching a maximum figure-of-merit value of 0.81. Hence, proving the ability of graphene to enhance the thermoelectric properties of the sample under study.

DEDICATION

To my mother, for her love and her constant motivation for me to finish my degree.

To my father, for his trust and the high expectations he has for my future.

To my siblings, to Ahmed, Haneen, Fatoom and Ibrahim.

To my friends, for the comfort, for the fun, for the sincere conversations, for the love, to Anwar, Fatoom, Hebba, Nada, Mona and Shoug.

To my other part, my journey friend, for the kindest soul, Hira. For making this experience special, bearable, and beautiful.

ACKNOWLEDGMENTS

I would like to acknowledge my supervisor Dr. Khaled Youssef, for giving me the opportunity to do my thesis under his supervision and for his constant academic guiding and support.

Special thanks to Ms. Hira Khalil, for drawing the structure of bismuth-telluride.

I also would like to acknowledge my thesis committee members, Dr. Ahmed Abdala, Dr. Andre Mkhoyan, and Dr. Ahmad Ayesh, for their comments and advice.

Special thanks to the Centre of Advanced Materials and the Central Laboratory Unit at Qatar University for their assistance in conducting the experimental work. Specifically, Dr. Peter Kasak, Mr. Abdulla Al Ashraf, Mr. Mohammed Saleh, Mr. Moinuddin Yusuf, Mr. Abdul Jaleel Naushad, Mr. Essam Attia, Ms. Noora Al Zaidan, Dr. Ahmed Abd-Elsalam, and Dr. Mohammed Yousuf.

Thanks to the external examiner, Dr. Khaled Mahmoud, for his valuable and appreciated comments on the thesis. And finally, I would like to thank the faculty members at the Materials Science and Technology Master Program who taught me many valuable courses throughout my Master of Science study.

TABLE OF CONTENTS

LIST OF TABLES

LIST OF FIGURES

CHAPTER 1: INTRODUCTION

Thermoelectric Materials

Thermoelectric materials can decrease energy consumption by converting waste heat into electrical energy without the need for bulk fluids or moving parts. A typical thermoelectric device consists of two conducting materials joined through a junction. One of the conducting materials has negative charge carriers (e.g., electrons) and referred to as n-type, whereas the other has positive charge carriers (e.g., holes) and called p-type. Once a temperature gradient is provided through the opposite ends of the device, carriers diffuse from the hot to the cold side, producing electricity (Figure 1). This electric potential produced, which resulted from temperature difference, is known as the Seebeck effect. The most famous examples of thermoelectric materials include bismuth telluride, lead telluride, sodium cobaltate, tin selenide, and silicon germanium, which are used in applications like lasers, computer chips, and infrared detectors. However, the low efficiencies of the commercial thermoelectric materials restrict their usage greatly.

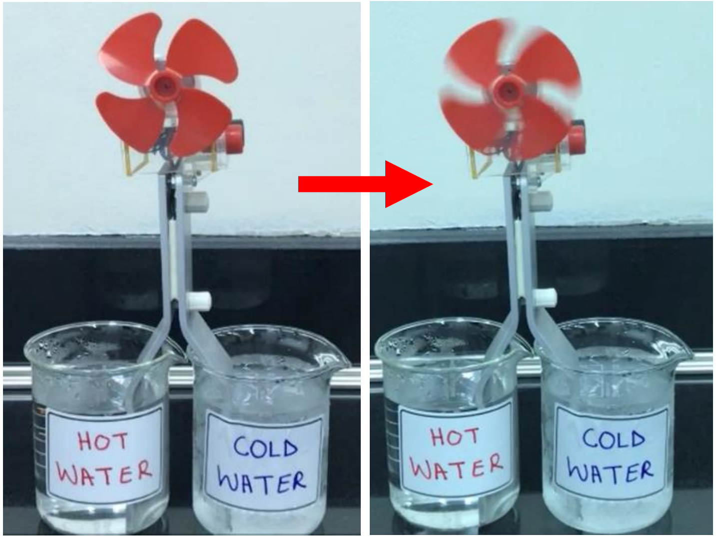

Figure 1: Thermoelectric fan running by providing a temperature gradient.

Thermoelectric Properties

The characterization of a thermoelectric device's performance is assessed through the value of the figure of merit (ZT), which is defined as:

$$ZT = \frac{S^2 \sigma \, T}{\kappa} \tag{1}$$

where S is the Seebeck coefficient, σ is the electrical conductivity, T is the absolute temperature, and κ is the total thermal conductivity. The total thermal conductivity consists of the summation of both electronic (κ_E) and lattice (κ_L) thermal conductivities, and the term $S^2\sigma$ is known as thermoelectric power factor (PF).

Electrical Conductivity

The electrical conductivity directly depends on the charge carrier mobility (μ), charge carrier concentration (n) and charge of the carrier (e), which are a consequence of the electrical band structure of the material, as in equation (2):

$$\sigma = ne\mu \tag{2}$$

Moreover, mobility of charge carrier composes of the mobility of the carriers in the matrix (μ_{matrix}) and the mobility of carriers at the interface ($\mu_{interface}$), as shown in equation (3):

$$\frac{1}{\mu_{Total}} = \frac{1}{\mu_{matrix}} + \frac{1}{\mu_{interface}} \tag{3}$$

and the mobility at the interface is defined as:

$$\mu_{interface} = Le\left(\frac{1}{2\pi m^* k_B T}\right)^{\frac{1}{2}} \exp\left(-\frac{E_B}{k_B T}\right) \tag{4}$$

where L, m^*, k_B, T, and E_B, are the distance between two adjacent interfaces, the effective mass of the carrier, Boltzmann constant, the absolute temperature, and the potential barrier height, respectively [1]. From equation (4), it is noticed that high temperatures will lower the mobility at the interface, hence reducing μ_{total}.

Seebeck Coefficient

Seebeck coefficient, in contrary to electrical conductivity, is inversely proportional to the concentration of carriers, as presented in equation (5):

$$S = \frac{8\,\pi^2 k_B^2}{3\,e\,h^2}\,m^* T (\frac{\pi}{3n})^{\frac{2}{3}} \tag{5}$$

where h is Planck’s constant [2]. This is why the prior two thermoelectric parameters usually have opposite effects on the thermoelectric material.

Thermal Conductivity

The total thermal conductivity consists of the electronic (k_E) and the lattice (k_L) thermal conductivities and can be calculated using density (ρ), thermal diffusivity (D), and specific heat (Cp) values of the material as in equation (6):

$$k_{Total} = k_E + k_L = D\rho C_p \tag{6}$$

Moreover, electronic thermal conductivity can be found using Wiedemann-Franz law:

$$k_E = \sigma T L \tag{7}$$

where L is the Lorentz number (with a value of 1.7×10^{-8} V^2K^{-2}) [3]. The lattice thermal conductivity is usually calculated after finding k_{Total} and k_E, and depends on various parameters including phonon velocity and phonon relaxation time. Therefore, the electrical conductivity and phonon scattering affect the total thermal conductivity. Hence, the thermal conductivity is linked to the first thermoelectric parameter as well.

Enhancing the figure of merit can be done by raising the power factor value and/or reducing the overall thermal conductivity. Despite a large number of thermoelectric materials studied, the ZT value of existing commercial materials is very low, where bismuth-telluride-based alloys remain very critical for near room-temperature applications [4].

Preparing bismuth telluride materials through recent nano-based techniques have given new opportunities to further enhance its thermoelectric properties. Even though high ZT values of nearly 1.5 for p-type antimony doped bismuth telluride have been reported [5, 6], its commercial applications is greatly restricted by its n-type counterpart, selenium doped bismuth telluride, that shows much inferior thermoelectric performance of ZT less than 1 at room temperature [7]. Therefore, there is a need for further improvements in the n-type of this alloy. Based on several studies, the enhancement of the ZT of thermoelectric materials could be possible through nanostructuring as well as nanocompositing. Introduction of a nanofiller, such as two-dimensional graphene, to an optimized nanostructured bismuth telluride, can further enhance the thermoelectric performance through improving the electrical conductivity as well as phonon scattering [8, 9].

Ball milling is a considerably cheap and industry applicable nanostructuring technique that is proved to show an increase in the figure-of-merit value [10]. However, optimizing the milling time is critical in order to obtain better materials. Moreover, optimizing the nanofiller used is essential to tune and understand the effect of graphene on the studied alloy. Various factors can affect the performance of graphene nanofiller, such as processing time, amount, and type. For instance, different graphene types can have different effects on the thermoelectric properties of the doped alloy. Pristine graphene of micro-size sheets tends to mostly increase the electrical conductivity [11]. However, graphene quantum dots, nanosheets, and nanoribbons would have better ability to increase scattering and lessen the thermal conductivity of the alloy, while still showing improvements in electrical conductivity [12-14]. Moreover, the mixing technique of graphene with thermoelectric alloy might be essential in tuning the nanostructure, as premixing graphene with the dopant may allow the graphene to concentrate on the grain boundaries of the material.

The main goal of this research is to synthesis a highly effective n-type bismuth telluride with graphene nanosheets of a composition Gr-$Bi_2Te_{2.7}Se_{0.3}$, having a thermoelectric ZT value above 1. This is proposed to be achieved through two main techniques, first by optimizing the nanostructured n-type bismuth telluride alloy through ball milling, followed by the addition and optimization of different concentrations and addition times of graphene nanosheets in order to boost the thermoelectric properties and reach the desired ZT value.

Therefore, the hypothesis of this work is that reducing the grain size through nanostructuring and introducing a nanofiller (graphene) by nanocompositing could be good approaches to enhance the final thermoelectric properties of the n-type $Bi_2Te_{2.7}Se_{0.3}$.

Research Questions

The main questions targeted in this research are:

- How is the structure of $Bi_2Te_{2.7}Se_{0.3}$ nanocomposites affected by graphene concentration and addition time?
- How is the graphene nanosheet addition able to affect the thermoelectric figure of merit of n-type $Bi_2Te_{2.7}Se_{0.3}$ alloy?

CHAPTER 2: LITERATURE REVIEW

Bismuth Telluride As A Thermoelectric Material

Bismuth telluride (Bi_2Te_3) has a layered rhombohedral crystal structure and is one of the most vital systems utilized for low-temperature applications, typically below 250 ºC [15]. Its structure results in high mobility of charge carriers, accompanied by low lattice thermal conductivity, making it a good thermoelectric material. Along the c-axis, bismuth and tellurium atoms are layered as Te-Bi-Te-Bi-Te, in the way presented in Figure 2 [16, 17]. Two types of Te atoms exist, Te1 which is bonded to Bi atoms from one side and other Te1 atoms from the opposite side, and Te2, which is only bonded to Bi atoms from both sides. One property of this system is its capability to maintain its symmetry with doping. Doping bismuth telluride with selenium (Se) or antimony (Sb) gives either electron or hole conducting thermoelectric materials. For these alloys, the optimized compositions for the n- and p- types are $Bi_2Te_{2.7}Se_{0.3}$ and $Bi_{0.5}Sb_{1.5}Te_3$, respectively.

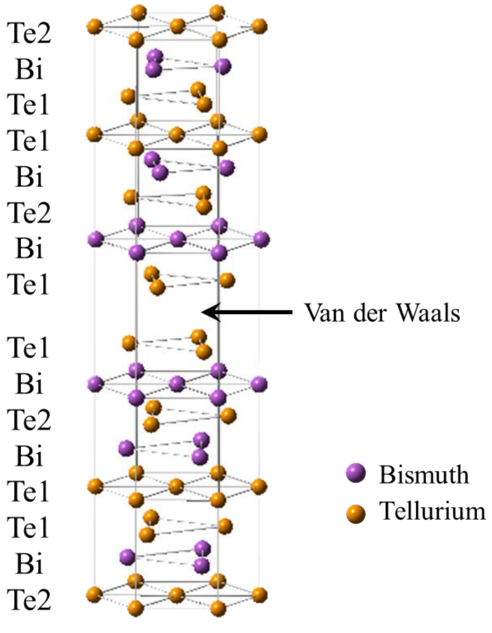

Figure 2: Crystal structure of bismuth telluride.

Properties of Doped Bismuth Telluride

One limit of bismuth telluride is the small bandgap of 0.14 eV, which leads to the undesirable effect of activation of minority charge carriers [18]. This effect could be reduced by increasing the size of the bandgap through doping. However, the doping effect on the thermoelectric properties of bismuth telluride shall be considered as well. One main challenge in n-type doping is the selective behavior of Se in Te2 sites, which results in an anisotropy of transport properties. The thermal conductivity, for instance, is double at ab-planes compare to the c-axis, whereas the electrical conductivity is 3-7 times higher along ab-planes compared to c-direction. This contracts the p-type alloy where there is no preference in Bi and Sb sites, making the alloy isotropic. This is why doped p-type shows better improvements in ZT values, compared to doped n-type, which requires additional processing to orient the grains for maximized performance.

Nanostructuring

Materials that have at least one dimension in the range of 1 and 100 nm are referred to as nanostructures. Nanostructures grant exclusive and specific features to materials while conserving their bulk properties. Due to the high surface area of these structures, nanomaterials have high-performance applications as they play a critical role in the advancement of technologies. Thus, the interest in nanostructures has increased in the last years in electrical, biological, chemical, physical, and optoelectrical based fields.

Exclusive features generated at the nanoscale are due to the electron confinement in space, and they greatly depend on the material’s dimensions. Recently, studies have been successfully enhancing the thermoelectric properties of bismuth telluride alloys and considerably increasing the figure-of-merit through nanostructuring [10]. The reason behind the enhancement of ZT values within nanostructured bulk thermoelectric materials is the increased density of grain boundaries and interfaces. These act as an essential factor for improving the scattering of phonons by causing a decrease in the lattice thermal conductivity, thus boosting the figure of merit value.

Generally, there are two approaches for nanostructuring, either top-down or bottom-up. The prior approach relies on splitting a bulk material into the nanoscale, whereas the latter approach builds up the material by joining atoms or molecules together. Analysis of the characterization of Bi_2Te_3 thermoelectric materials prepared by such approaches has already been done by many studies. For example, Takiishi et al. [19] developed nanocrystalline thin films of n-type bismuth telluride using flash evaporation as a bottom-up technique. The thermal conductivity of the films prepared was reduced by 50% compared to the bulk material. Moreover, Fan et al. [20] studied the effect of nano inclusions on ZT value of bismuth telluride nanocomposites prepared via melt spinning as a top-down method. Researchers proved that increasing the weight of nano inclusions within the thermoelectric material reduces its thermal conductivity and thus retains a higher figure-of-merit value.

Ball Milling

One top-down technique of nanostructuring is ball milling, which uses mechanical energy to grind the material into smaller pieces. It is considered a powerful dry powder processing technique for producing alloys and solid solutions in nano-size. Nevertheless, the main aim of the mechanical milling (MM) process is grain refinement or/and phase transformation. Grain refinement occurs as a result of severe plastic deformation of repeated mechanical impacts, as shown in Figure 3. Milling should be performed until the time necessary for the initial material to reach a steady state. Then, the resulted power is compacted into bulk materials through heat treatments in order to study the microstructure and properties. The main components of a MM process are the initial raw materials, the mechanical mill, and the used process variables.

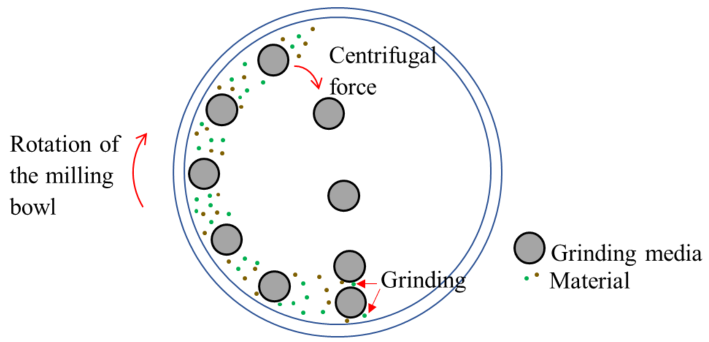

Figure 3: Dynamics of Ball Milling.

The initial raw powders can include metals, alloys, or refractory compounds. Their size may range from 1-200 µm, but most importantly, the size of raw powders should be smaller than grinding medium (e.g., grinding balls). Using high purity powders is necessary as they decide the final composition, phase, and kinetics. In addition, there are several types of high-energy mills available, and they mainly differ in their capacity, design, and efficiency. The most used shaker mills in laboratories are SPEX mills, which move back-and-forth along with lateral motions up to a thousand times per minute [21]. The vials and grinding medium used are typically made out of metals or ceramics. It is reported that the produced nanomaterials through ball milling tend to decrease thermal conductivity while maintaining good electron transport features [22].

Compositing

Compositing is when different materials are homogeny mixed together in order to produce a single material without physical blending. The created material has a combination of unique features that did not exist in any of the single materials.

Generally, composite materials are comprised of a matrix and a filler. Compositing has been proved to enhance the thermoelectric properties of materials. Moreover, using different fillers along with bismuth telluride as a matrix is reported to cause a reduction in the overall lattice thermal conductivity [23]. This decrease is due to the new interfaces formed between the filler and the matrix. In addition, these interfacial areas are also reported to enhance the Seebeck coefficient value by carrier filtering or quantum confinement mechanisms [24].

Nanofillers

Almost all fillers used for compositing semiconductor thermoelectric materials are nanosized (<100nm) since they give the possibility to tune the thermoelectric properties once they are controlled at the nanoscale. Moreover, according to the number of dimensions of a material that are in the nanoscale, nanofillers are distinct into several groups as discussed below.

Zero dimensional fillers (0DFs) have all three dimensions of the material within the nanoscale [25]. Numerous studies have used 0DFs with n-type bismuth telluride matrix, either doped or undoped, revealing different results. Zhang et al. [26] employed silver (Ag) nanoparticle prepared via polyol reduction of silver nitrate as a filler for undoped Bi_2Te_3 powders. The Ag nanoparticles were uniformly dispersed in the grain boundaries creating lots of defects and interfaces, hence forming a two-phased heterostructure inside the matrix. This resulted in a significant reduction in the lattice thermal conductivity and also suppressing grain growth, hence improving the ZT value from 0.19 to 0.77 at 475 K. Moreover, Li and Liu [27] utilized mechanical milling as a mixing technique to synthesize SiC/Bi_2Te_3 nanocomposite. Their optimized concentration of the SiC was 0.1 wt.%, and it enhanced the ZT by 17%, reaching a value of 0.66 at 440 K. On the other hand when

0DFs were used with doped n-type bismuth telluride, the thermoelectric properties were deteriorated. Jiang et al. [28] produced a ZnO/ $Bi_2Te_{2.7}Se_{0.3}$ nanocomposite by ball milling and noticed a high increment in electrical conductivity accompanied with a high reduction in Seebeck coefficient, hence resulted in a drop of the final ZT value from 0.6 to 0.5. In another study by Liu et al. [29], the addition of SiC 0DF to n-type doped bismuth telluride did not improve the ZT value for all the prepared concentrations. This was reasoned as the lessening in thermal conductivity was not enough to pay off the decrease in power factor. The highest reduction of ZT reached was for the 1% SiC at 423 K from 1.11 to 0.38. In addition, there were other studies of 0DFs with undoped bismuth telluride matrix which caused lowering in ZT. The used nanofillers in these cases were graphite powder [30], fullerene (C60) [31], amorphous carbon [32], and rice like polyaniline [33]. **Generally**, the ZT of undoped bismuth telluride pristine is lower than the doped and based on the literature, 0DF composites along with doped $Bi_2(TeSe)_3$ do not show improvements in final ZT values.

One dimensional fillers (1DFs) own two of the total three dimensions within the nanoscale range [25]. Based on the available studies, it is noticed that using both doped and undoped n-type bismuth telluride matrix can give enhancements in ZT values of composites with 1DFs. Kim et al. [24] used chemical vapor deposition to prepare a composite of multiwall carbon nanotubes and undoped Bi_2Te_3. The research group obtained 63% improvements in ZT with an optimized value of 0.85 at 473 K. Many other studies used the same 1DF as well with an undoped matrix and obtained noticeable improvements in the thermoelectric properties. The employed mixing techniques include polyol reduction [34], hydrothermal [35], and ultra-sonification [36]. Moreover, single-wall carbon nanotubes were used by Zhang et al.

[37] along with an undoped matrix resulting in improvements in ZT from 0.99 to 1.28 at 420 K with 0.5 wt.% filler concentration. Whereas, another study utilized the same type of matrix and filler but resulted in lower ZT value for the composite compare to the base [32]. The ZT at room temperature was 0.23 for 0.15 wt.% filler and 0.32 for the pristine sample. Other studies, who used doped bismuth telluride, mostly employed multiwall carbon nanotubes as a filler. Park et al. [38] used a composition of $Bi_2Te_{2.7}Se_{0.3}$ and a concentration of 0.015 vol.% filler gaining an enhancement in ZT value from 0.88 to 0.98. On the other hand, when Lognone and Gascoin [23] used a matrix composition of $Bi_2Te_{2.4}Se_{0.6}$, lower ZT value of 0.25 was obtained for the composite compared to the base with ZT of 0.52 at room temperature. Even though there are more studies on the undoped n-type matrix, there are some of the published doped studies with 1DF, which showed improvements in ZT.

Two-dimensional fillers (2DFs) have only one dimension within the nanoscale range [25]. Most 2DFs for undoped n-type bismuth telluride focus on graphene regardless of the form, and there are no studies that show the effect of graphene on doped bismuth telluride. In addition, one study used polythiophene nanosheet as a 2DF with a doped matrix but showed a reduction in all ZT values for all concentrations prepared due to the low electrical conductivity of the filler [39].

Graphene is the most famous two-dimensional nanofiller that has become an attractive research topic since its first successful isolation [40]. Graphene is a planer structure of carbon where the atoms share their sp^2 electrons with three other neighboring carbons, forming a honeycomb network (Figure 4). The covalent bond, formed by the hybridization of sp^2 orbitals, gives graphene remarkable mechanical properties of tensile strength around 130 GPa and Young’s modulus about 1 TPa, making it stronger than diamond [41]. Moreover, graphene possesses extraordinary thermal and electrical properties that can be further tuned through physical and chemical means. Graphene has a zero-band gap with a remarkably high concentration of charge carriers at room temperature with mobility that reaches up to 40,000 $cm^2/V.s$, superior electrical and thermal conductivities about 200 S/m and 2800 W/m.K, respectively [41].

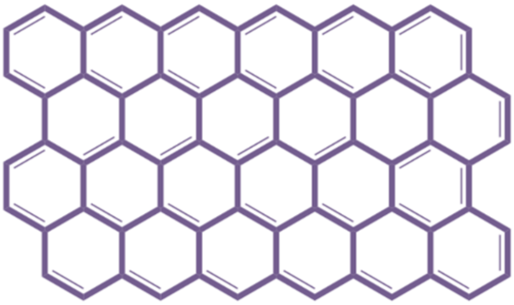

Figure 4: Graphene monolayer structure

For thermoelectric materials, the high thermal and electrical conductivity combination of pure graphene is undesirable. However, the addition of graphene to semiconductors or insulators can enhance their electrical conductivity by orders of magnitude even at loadings of less than 0.1 vol% [42]. On the contrary, its compositing effect on thermal conductivity is less noticeable, and only high loading concentrations will result in a significant increase in its value [43]. Therefore, graphene as a filler can play a significant role in affecting the thermoelectric properties of composites, and optimizing its concentration is a must to achieve the desired characteristics.

Several articles studied the effect of graphene on the efficiency of thermoelectric materials, but these mainly suffered from the low ZT values (less than 1) of their initial thermoelectric materials. For instance, Liang et al. [44] tried to enhance the efficiency of undoped bulk n-type bismuth telluride materials by adding up to 2 vol.% graphene nanosheets using hydrothermal and spark plasma sintering methods. Even though the addition of graphene nanosheets raised up the ZT value by more than 30%, the maximum value achieved of ZT is 0.21, which is very low. Also, Li et al. [16] reached improvement of 50% of the ZT value for undoped n-type bismuth telluride crystals through doping with 5 vol.% graphene; still, the maximum ZT achieved was 0.45. Other studies used reduced graphene oxide nanosheets and got a final ZT lower than 0.4 despite the improvements of up to 60% due to graphene addition [1, 45]. Thus, the initial ZT value of the alloy is very critical, and doping an optimized n-type material with graphene is expected to be more efficient in boosting the thermoelectric characteristics and ZT value of the material.

CHAPTER 3: METHODOLOGY

Materials and Methods

Elemental powders of bismuth (99.999%, Alfa Aesar), tellurium (99.99%), and selenium (99.5%) were used to produce n-type bismuth telluride alloy. In the glove box under the argon atmosphere, the powders were weighted according to the formula $Bi_2Te_{2.7}Se_{0.3}$ and loaded into a stainless-steel vial. The powders were then milled in SPEX milling device (SamplePrep, 8000M) using a ball-to-powder weight ratio of 7:1 (Figure 5). Different mixing times of 4, 8, 12, 16, and 20 hours were carried out. Long milling hours are critical to ensure reaching a stable phase of nanosized particles.

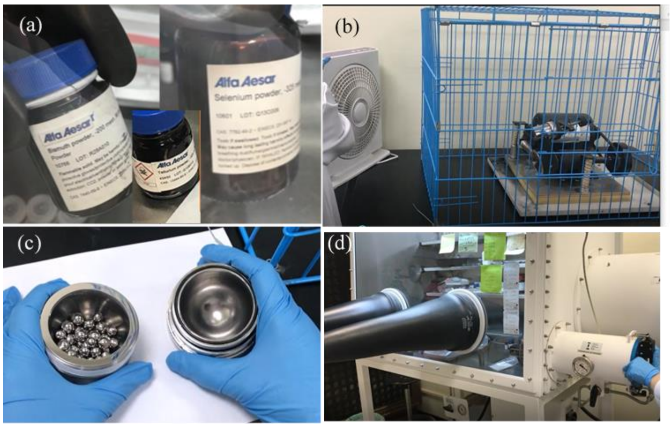

Figure 5: Preparation of n-type bismuth telluride samples for mechanical milling, (a) powders purchased (b) SPEX milling device (c) milling vial and (d) glove box.

Optimum milling time from the previous step was used to mill four graphene-based bismuth telluride composites ($Gr/Bi_2Te_{2.7}Se_{0.3}$) of different graphene weight percentages and addition times, as shown in Table 1. Graphene nanoplatelets used were purchased from Sigma-Aldrich company. All milling conditions were kept consistent as the pristine $Bi_2Te_{2.7}S_{0.3}$. The addition of graphene at the last phase of mechanical milling is expected to protect the very brittle graphene from fracturing and, at the same time, assure its even distribution into the grain boundaries of the nanostructured material. This entire step will help in understanding the structural stability of graphene and optimize its amount and addition to the alloy.

Table 1

Samples' Codes According to Graphene Addition Amount and Time

Sample Code	Graphene amount (wt.%)	Addition time
Gr 5 – 20 hrs	0.05%	at the beginning
Gr 5 – 10 min	0.05%	last 10 minutes
Gr – 10 min	0.5%	last 10 minutes
Gr 5 – 1 min	0.05%	last 1 minute

The compaction of powders was performed for all samples using the Spark Plasma Sintering (SPS) technique at 440 ºC and 45 MPa (setup shown in Figure 6). The temperature used was chosen based on the melting point of bismuth telluride, which is 580 ºC [45]. It is important to assure that sintering is done below the melting point of the material to allow bonding to take place through the diffusion of atoms. In addition, a high pressing pressure is used to ensure the final nanostructured bulk product has very minimal porosity and thus guarantee that the electrical conductivity of the material produced is not degraded.

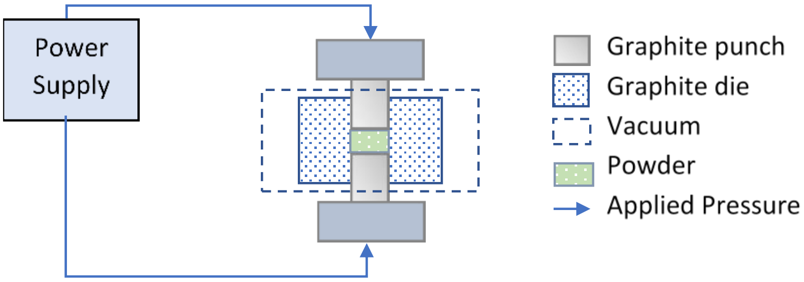

Figure 6: SPS device schematic.

Characterization

Characterization techniques are important to verify whether the produced product is correctly prepared and is able to serve its intended purpose. There are several standard techniques which are commonly used in Material Science field in order to investigate, study, measure and understand the structure and properties of the materials. Below are the characterization techniques implemented in this study.

Structural Characterization

X-Ray Diffraction (XRD) technique is most commonly used for identifying the crystal structure of unknown crystalline samples. It is a non-destructive analytical technique that uses X-ray waves to determine the crystal structure of metallic or ionic crystals. In addition, this technique can also be used to measure the average spacing between the layers of atoms, give an approximation for a grain size of material and find the strain in a material due to deformation**.**

The main parts of the XRD device are X-ray source, sample stage, and detector, as represented in Figure 7 (a). These parts are connected in a circular way such that when an incident ray comes out of the X-ray source, it will hit the sample and get diffracted an angle of 2 thetas of the original beam. Moreover, when an X-Ray is passed through the crystal, diffraction will occur at different angles, and these angles depend on the distances between atomic planes. When the hit planes are in phase (constructive), their energies are added, creating dark spots on the detector plate. Circular patterns are then created as a result of sample rotation, and their radius is used to calculate the distance between plates within the crystal structure. The intensities of X-ray beams at different diffraction angles are then captured and converted into a diffractogram. Using the outcome data, the distance between adjacent layers in a crystal (d) can be calculated and hence used to determine the size of the unit cell. Braggs Law is a derived equation for the relation between the wavelength of X-ray beam (λ) and d, which is given by:

$$\lambda = 2d\,sin\theta \tag{9}$$

where θ is the angle of incidence (angle between the X-ray beam and surface of the crystal). Figure 7 (b) shows a schematic for Braggs law origin, and it is only when an angle satisfies Braggs Law, diffraction occurs.

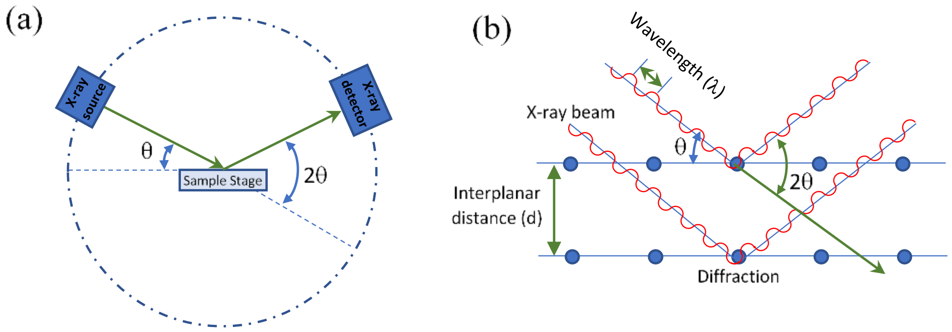

Figure 7: Schematic for (a) XRD setup and (b) Braggs law origin.

Moreover, the resulted peaks from an XRD diffractogram can also be used to calculate the grain size and lattice strain within the unit cell. There are many proposed models that rely on the fact that the width and intensity of the peaks are affected by the processing of materials. For instance, the introduction of strain and refinement of grain size due to the mechanical milling process broadens the XRD peaks and reduces their intensities [46]. Explained below are two-grain size calculation models that are used in this study.

Williamson-Hall method assumes that the broadening due to grain size and strain is an additive to the generated Bragg’s peak, with the strain being uniform in all crystallographic directions [47]. The resulted equation, according to this assumption, is:

$$\beta_{hkl} \cos\theta = \left(\frac{k\lambda}{D}\right) + (4\, \varepsilon \sin\theta) \tag{10}$$

where D is the grain size, ε is the strain, β_{hkl} is the width of the peak at the half-maximum intensity, and k is a constant. Linear fitting of data points from peaks into $(\beta_{hkl} \cos\theta)$ versus $(4 \sin\theta)$ plot results in a slope representing strain value and a y-intercept of a constant divided by interplanar spacing, as represented in Figure 8.

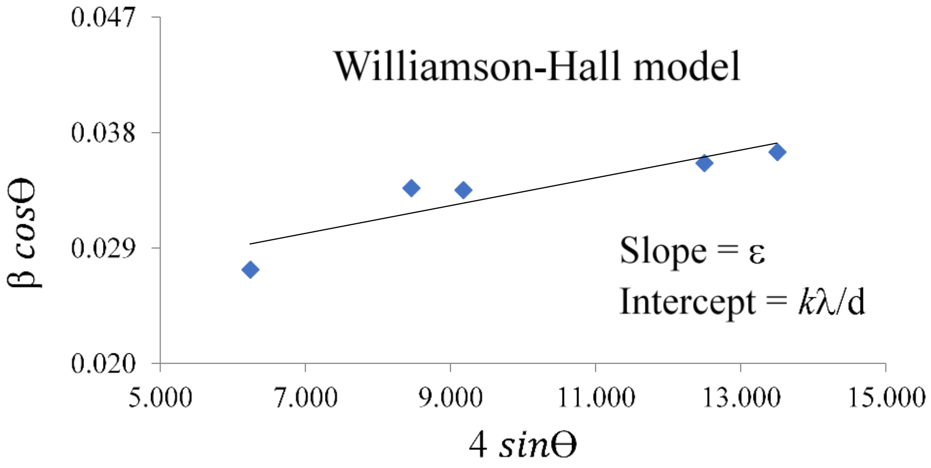

Figure 8: Williamson-Hall model for grain size calculation.

Warren-Averbach method is based on representing diffraction peaks using Fourier series to extract information about grain size and strain. Applying Cauchy and Gaussian functions lead to the following equation:

$$\frac{{\beta_{hkl}}^2}{\tan^2\theta} = \frac{\lambda}{D}\left(\frac{\beta_{hkl}}{\tan\theta \sin\theta}\right) + 25\, \langle \varepsilon^2 \rangle \tag{11}$$

where D is the grain size, ε is the strain and β_{hkl} is the width of the peak at half-maximum intensity [46]. Linear fitting of data points from peaks into $(\frac{{\beta_{hkl}}^2}{\tan^2\theta})$ versus $\left(\frac{\beta_{hkl}}{\tan\theta \sin\theta}\right)$ plot results in a slope representing a constant times strain value squared and y-intercept of a constant divided by interplanar spacing, as presented in Figure 9.

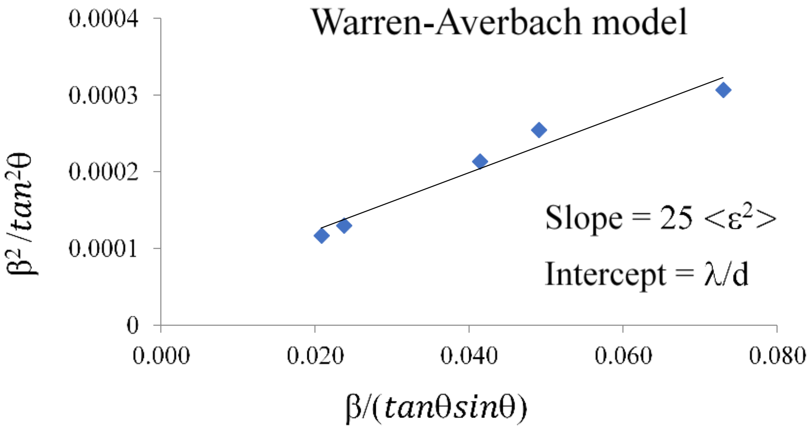

Figure 9: Warren-Averbach model for grain size calculation.

Scanning Electron Microscope (SEM) is typically used to study the surface morphology and topography of the material. The device consists of a 2-inch thermal gun, a tungsten bulb, the column of the microscope, and a sample introduction chamber. When a beam of electrons is generated by the tungsten bulb and goes through the chamber under vacuum, it scans the whole sample side to side and from top to bottom. Then, electrons of the sample are emitted differently depending on their interaction with the beam, as shown in Figure 10. The reflected part of the beam is detected by the secondary electron detector and is used to generate a detailed surface image of the sample.

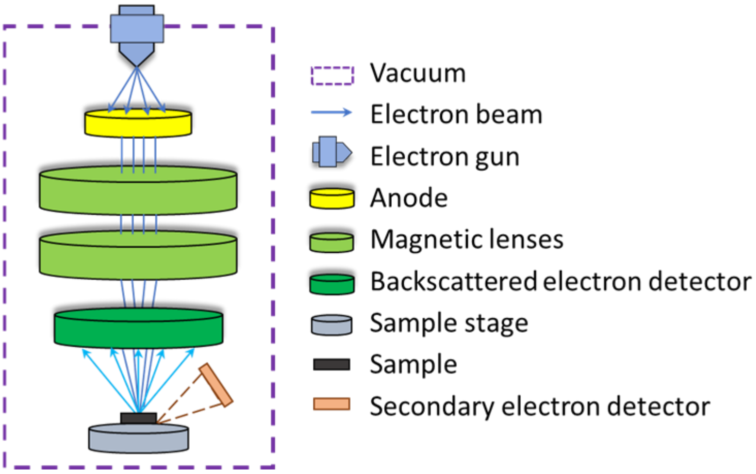

Figure 10: Scanning electron microscope device working principle.

Transmission Electron Microscope (TEM) is an advanced characterization tool of several techniques that is used to obtain information about the material at the atomic level. One highly utilized technique is imaging, which is used to gain information about the grain size and its distribution. The main results from this technique are the dark and bright-field images. The working principle of imaging depends on the interaction between an introduced electron beam and the sample to produce high-resolution images. For the bright field image, the objective aperture is used to allow only the direct beam to pass and interact with the sample. Whereas in dark field image, the aperture blocks the direct beam and allows the passage of diffracted beams only, as in Figure 11. The contrast of the resulted images depends on the phase and amplitude of the beam, which is a function of the type and thickness of the sample.

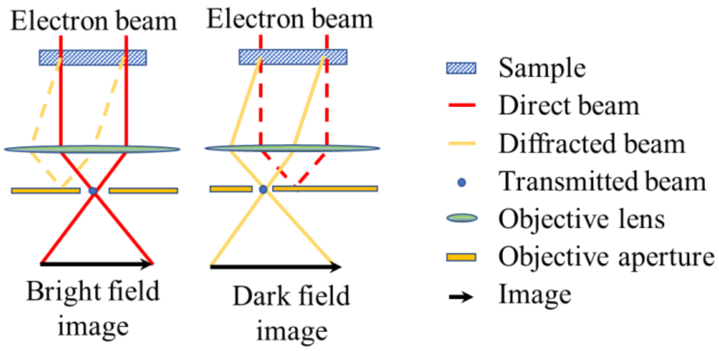

Figure 11: TEM imaging working principle for bright and dark field images.

Raman Spectroscopy helps in identifying elements/molecules in samples by giving the fingerprint of each element, depending on their Raman spectra. The main idea behind this technique is presented in Figure 12. Basically, the excitation of electrons within a sample via providing light energy (e.g., phonons) leads to Raman scattering, where the emission occurs at frequencies different from the incident frequencies. Stroke lines are the ones generated when the emitted frequency is less than incident ones, whereas anti-stroke lines are the ones generated at higher frequencies. By studying these stroke and anti-stroke lines, which are different for each element, the sample molecule can be identified. The concentration of these molecules in the sample can also be found from the intensity of the emissions.

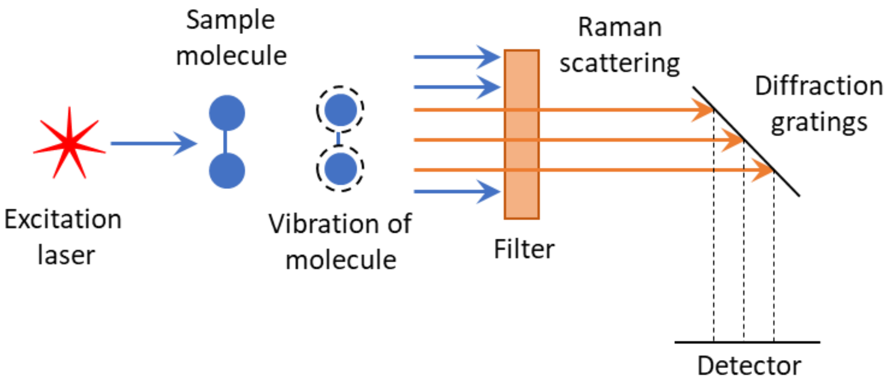

Figure 12: Raman Spectroscopy working principle.

Mechanical Properties Characterization

Vickers Hardness (HV) is a microhardness tester that is used to give an indication of the hardness of a material. The device uses a square trapezium diamond indentor that is used with a certain force and time to create indentions on the surface of the material, as represented in Figure 13. The depth of these indentations is then used to calculate the hardness based on the following equation:

$$\mathrm{HV} = \frac{0.1854\ \mathrm{F(kg)}}{\mathrm{d}_{\mathrm{avr}}^{2}(\mathrm{mm}^{2})} \tag{12}$$

where F is the applied force and d^2 is the area of indentation [48].

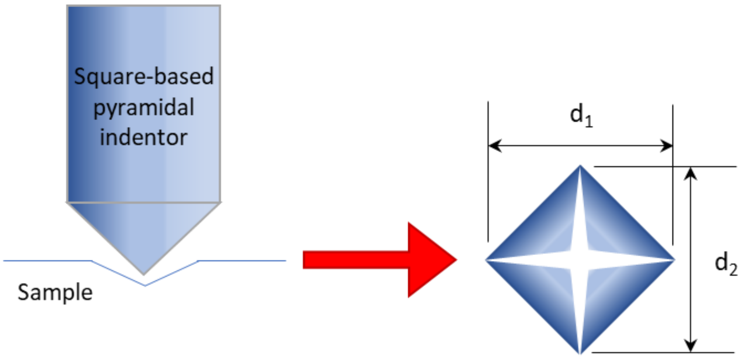

Figure 13: Vickers Hardness tester schematic.

Characterization of Thermal Energy

Differential Scanning Calorimetry (DSC) is a device that measures the energy released or absorbed during cooling or heating of a material. It is used to determine the thermal events of the sample, such as the enthalpy, melting, crystallization, and glass transition temperatures. The device contains a chamber with two heating metals inside, one for the sample, and the other is used as a reference, as in Figure 14. The reference and the sample pans are heated in separate means to maintain the temperature for both at the same degree, and the heat applied is recorded individually. The output from a DSC experiment is a graph of heat flow versus temperature.

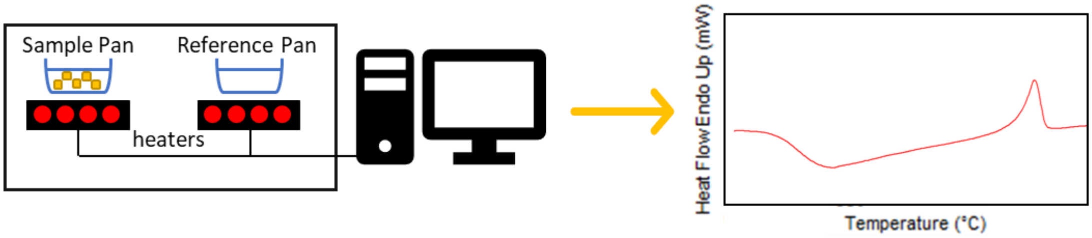

Figure 14: Differential Scanning Calorimetry working schematic.

Thermoelectric Properties Characterization

Seebeck coefficient and the electrical conductivity: There are several devices that can measure Seebeck coefficient or/and electrical conductivity parameters, but they differ in their working principles. The device utilized in this study is ‘SBA 485 Nemesis’ by NETZSCH company. This device is based on a four - points method, and its working schematic is shown in Figure 15. In SBA 485 Nemesis device, the sample is placed between a pair of micro heaters, thermocouples, and current pins. Seebeck coefficient measurement is done by generating cyclic heating from the microheaters working in alternation to produce a temperature gradient. The production of this temperature difference results in a voltage between the two thermocouples. These voltages are then measured and plotted against temperature difference, and from the slope of the fitting, the Seebeck coefficient is determined.

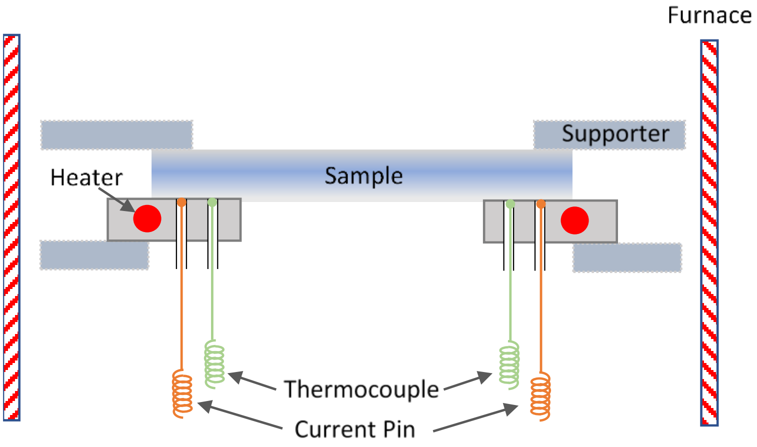

Figure 15: Schematic for the measurement setup of SBA 458 Nemesis device.

Besides, electrical conductivity value is obtained using the same device by applying different currents via the two current pins and then measuring the resulted voltage across the two ends of the sample.

Thermal conductivity. Light Flash Apparatus (LFA) represents an effective technique for measuring thermophysical properties, such as thermal conductivity. One device that uses this technique is 'LFA 467 Hyper Flash' by NETZSCH company. LFA is a non-destructive and fast technique with a simple working principle, presented in Figure 16. Basically, one surface of the sample is heated by providing a light pulse of short energy. The resulting temperature is then measured from the other side with an infrared detector. Specific heat and thermal diffusivity are then determined and used to calculated thermal conductivity (λ) by:

$$\lambda(T) = a(T)\,\rho(T)\,C_p(T) \tag{13}$$

where a is the thermal diffusivity in mm^2/s, ρ is the sample density in g/cm^3 and C_p is the specific heat in J/(g.K).

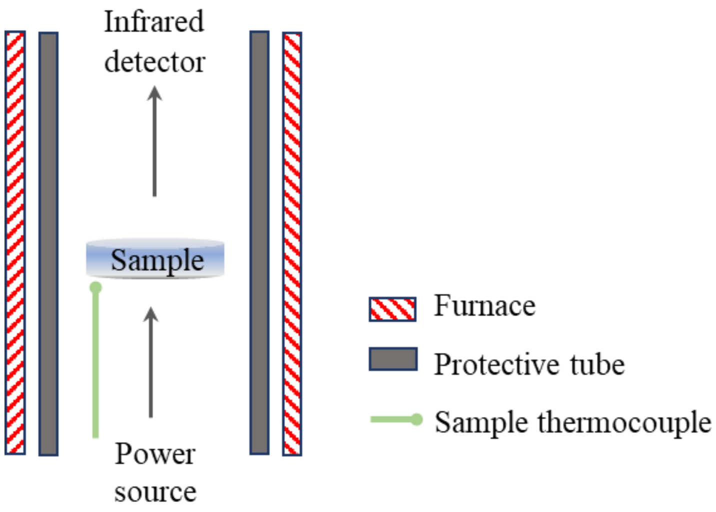

Figure 16: Schematic of the measurement setup for LFA 467 HyperFlash device.

Purpose of Characterization

The microstructure was continuously checked during processing and after finalizing the discs. For instance, the structure was checked during milling of pristine n-type bismuth telluride at 4, 8, 12, 16 and 20 hours, and was checked for as milled graphene-based composite powders and the sintered ones. The characterization included XRD (PANalytical, EMPYEAN), SEM (Nano-SEM Nova 450, FEI-USA), and HV (Future-Tech, FM-ARS900) as they can be an indication of the grain size and assure the purity and correct preparation of samples. Moreover, to further assure a precise calculation of final product grain size, transmission electron microscopy TEM (FEI Titan™ 60-300) was utilized on one of the composite samples.

In addition, Raman Spectroscopy (Thermo Fisher, DXR) and DSC analysis (PerkinElmer, DSC 4000) were performed for the as the milled optimum pristine sample as well as the graphene-based composites. Raman spectroscopy was used in order to check the crystallinity of graphene after milling and to study the effect of milling time on its structural stability, while DSC was done in order to further understand the thermal stability of the samples.

The prepared discs were used to study the thermoelectric properties of the optimized $Bi_2Te_{2.7}Se_{0.3}$ alloy and the final graphene/$Bi_2Te_{2.7}Se_{0.3}$ composite samples. Seebeck coefficient and electrical conductivity were measured using SBA 485 Nemesis device (NETZSCH), whereas thermal conductivity was measured using LFA 467 Hyper Flash device (NETZSCH).

All these different characterization techniques aided in optimizing the concentration of graphene and its addition time into $Bi_2Te_{2.7}Se_{0.3}$ alloy. They also helped in gaining more knowledge about graphene’s ability to tune the Seebeck coefficient, as well as the electrical, thermal and mechanical properties, thus fulfilling the objective of the research.

CHAPTER 4: RESULTS AND DISCUSSION

Prepared $Bi_2Te_{2.7}Se_{0.3}$ Powders

After performing mechanical milling, the purity of powders was checked by XRD. Figure 17 shows the diffraction patterns of pristine $Bi_2Te_{2.7}Se_{0.3}$ nanopowders milled for 4, 8, 12, 16, and 20 hours. As shown, all peaks match the reference code 98-024-7619 [49], hence no contamination is present, and the composition was successfully prepared. XRD data were also used to estimate the grain size of the samples using Warren-Averbach and Williamson-Hall methods and the final data is listed in Table 2. According to these results, Averbach is a better fit of higher regression values, and 20 hours milling shows lowest grain size for the nanopowders of 19 nm, hence the optimum milling time.

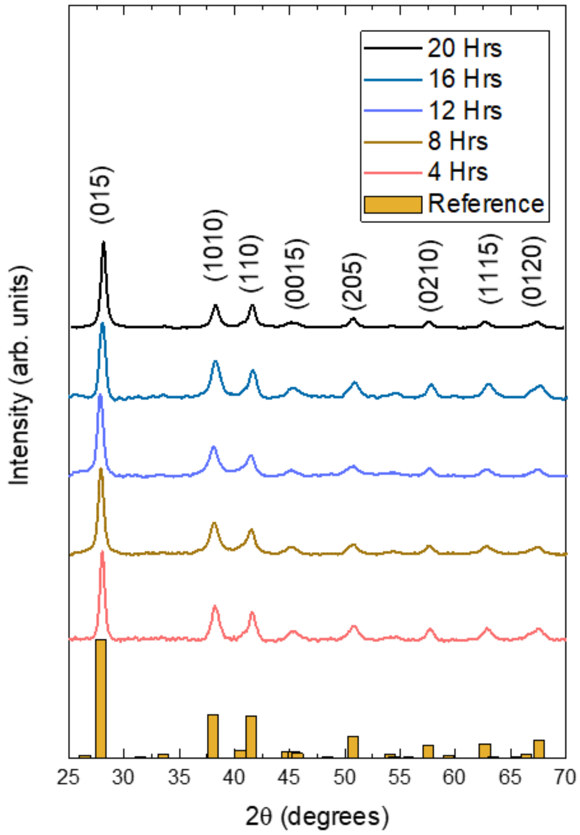

Figure 17: XRD peaks for $Bi_2Te_{2.7}Se_{0.3}$ nanopowders milled for different hours.

Table 2

Grain Size of $Bi_2Te_{2.7}Se_{0.3}$ *Nanopowders Milled for Different Hours*

Sample Code	Grain Size (nm)			
Milling hours	Averbach	R^2	Williamson-Hall	R^2
4	20.23	0.73	27.99	0.20
8	21.28	0.80	31.91	0.21
12	19.64	0.82	26.34	0.09
16	19.57	0.84	27.48	0.29
20	18.55	0.81	24.80	0.48

Hardness was also performed to further confirm the optimum sample and the results are shown in Figure 18. The highest HV value is 1.63 ± 0.05 GPa for 20 hours milled sample (N-20 hrs), and as the figure shows, the curve is becoming plateau at the last couple of measurements, implying that optimum millings hours are reached. Having high hardness is important for application purposes. Hence, XRD and hardness results suggest that the optimum milling hours for the n-type bismuth telluride understudy to produce the smallest $Bi_2Te_{2.7}Se_{0.3}$ nanopowders with high hardness value is 20 hours.

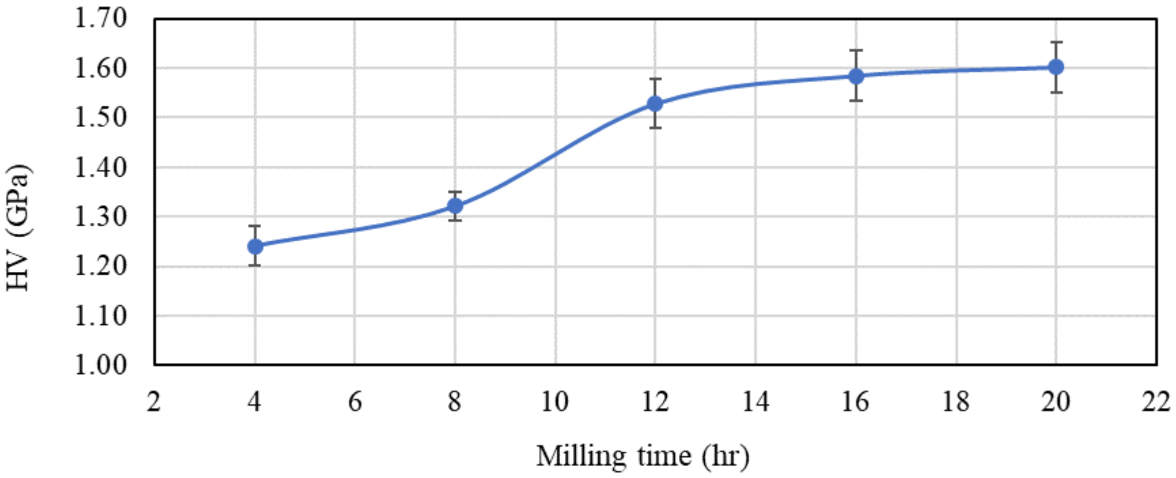

Figure 18: Hardness trend for $Bi_2Te_{2.7}Se_{0.3}$ milled for 4, 8, 12, 16 and 20 hours.

Prepared Gr/$Bi_2Te_{2.7}Se_{0.3}$ Composites

The optimum milling time of 20 hours was used to produce Gr/$Bi_2Te_{2.7}Se_{0.3}$ composites listed in Table 1. The as milled composites were characterized with XRD, hardness, SEM and Raman Spectroscopy, to confirm their purity, study their structure and surface morphology. Figure 19 shows the XRD peaks for Gr/$Bi_2Te_{2.7}Se_{0.3}$ composites. All composites had one phase and their peaks matches the reference of the pristine sample. No peaks for graphene are visible since it was only added in small amounts. Using data from XRD peaks, grain size was estimated and showed better fitting for Warren-Averbach model. Since grain size depends mainly on the milling time and all samples had the same milling hours, all are expected to have similar grain size. This is confirmed from Averbach results in Table 3 as the average grain size for all samples is found to be 16.89 ± 1.3 nm.

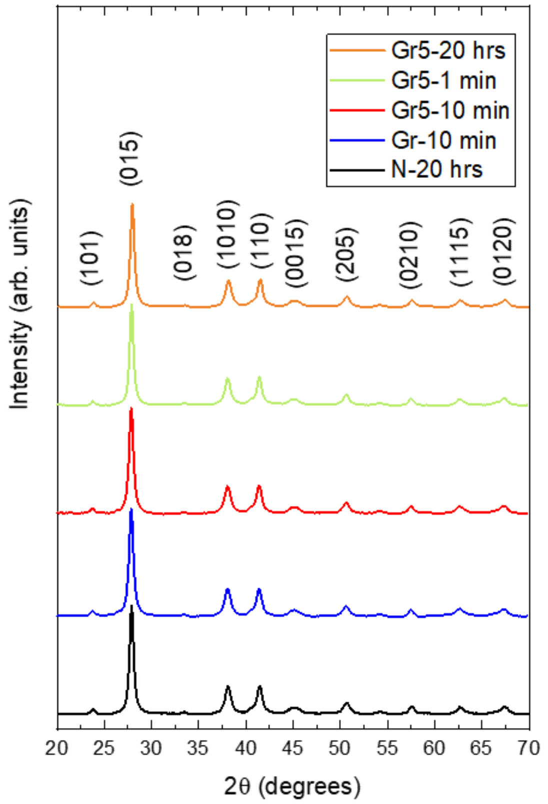

Figure 19: XRD peaks for Gr/$Bi_2Te_{2.7}Se_{0.3}$ composites.

Table 3

Grain Size of Gr/$Bi_2Te_{2.7}Se_{0.3}$ *Nanocomposites*

Sample Code	Grain Size (nm)			
Milling hours	Averbach	R^2	Williamson-Hall	R^2
Gr-10 min	16.30	0.91	19.48	0.40
Gr5-10 min	15.42	0.95	15.96	0.40
Gr5-1 min	17.51	0.91	18.75	0.45
Gr5-20 hrs	18.33	0.87	23.33	0.55

Moreover, Hardness values for the optimum pristine, as well as all composites samples, are shown in Figures 20. The main trend observed is that samples with lower graphene concentration of 0.05 wt.% had lower hardness values of an average of 1.53 ± 0.03 GPa compared to pristine of 1.63 ± 0.05 GPa whereas higher graphene concentration of 0.5 wt.% in Gr-10 min sample resulted in a much higher hardness compared to pristine. Therefore, the HV value for the N-20 hrs sample is in between the other two concentrations. Hence, graphene has the ability to control the hardness of the composite understudy, as small amounts (e.g., 0.05 wt.%) can lower the hardness value and higher amounts (e.g., 0.5 wt.%) can increase hardness values significantly.

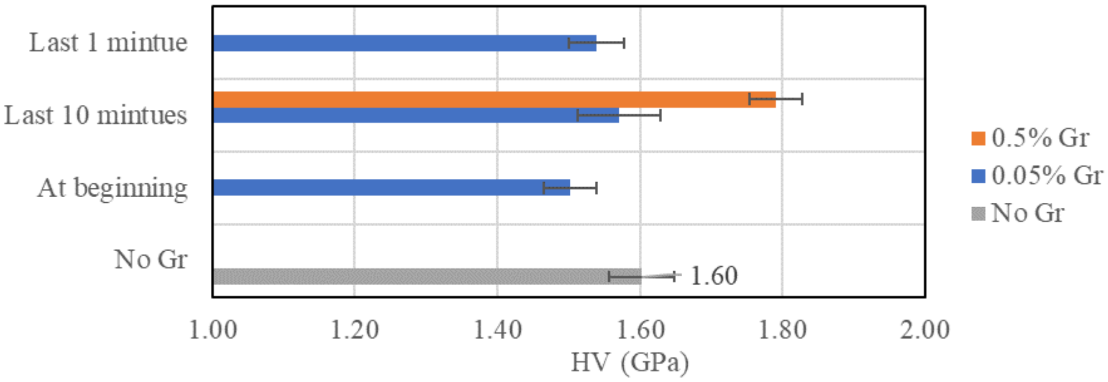

Figure 20: Hardness trend for Gr/$Bi_2Te_{2.7}Se_{0.3}$ composites.

The surface morphology of the composites can be understood from SEM results shown in Figure 21 (a) N-20 hrs (b) Gr-10 min, (c) Gr5-10 min, (d) Gr5-1 min, and (e) Gr5-20 hrs. The first thing to notice is the agglomeration of the nanoparticles in all samples. Agglomeration is common in nanomaterials since small-sized particles has a very high specific area (surface area to volume ratio), leading to a change in the dominant forces acting on the material [50]. Hence, the existing weak forces of Van der Waals have more effect on the nanoscale, causing agglomeration compared to the same bulk materials.

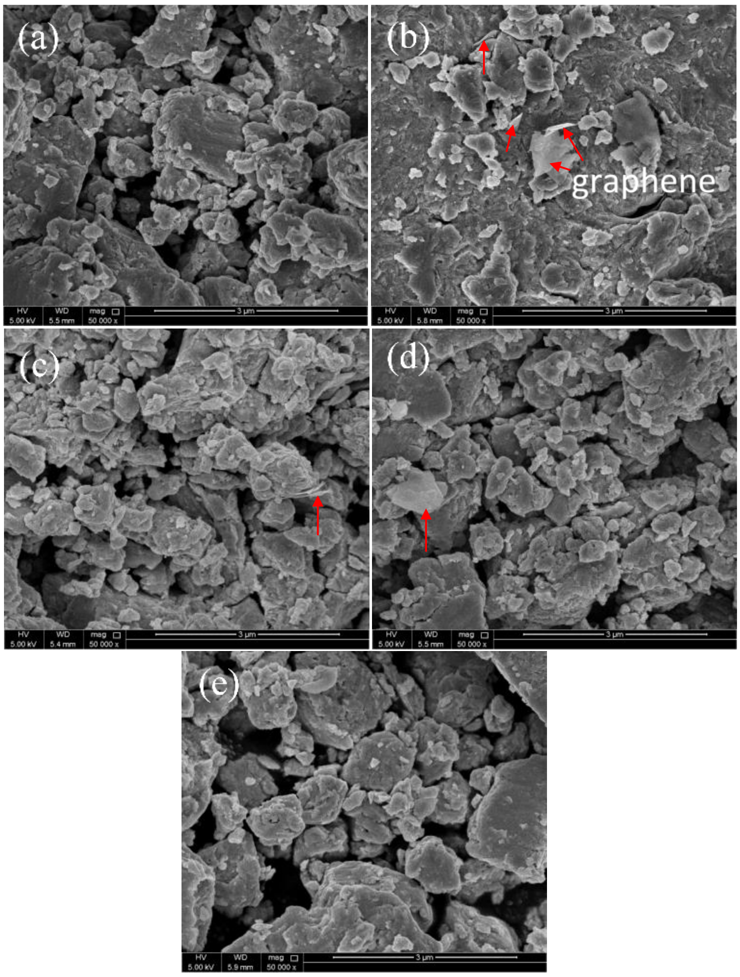

Figure 21*:* SEM images for (a) N-20 hrs (b) Gr-10 min, (c) Gr5-10 min, (d) Gr5-1 min and (e) Gr5-20 hrs.

Moreover, Figure 21 (a) shows the pristine $Bi_2Te_{2.7}Se_{0.3}$ sample showing the only agglomeration of nanoparticles. However, Figures 21 (b) - (d) show graphene 2D nanosheets within the composite (marked with red arrows). More graphene nanosheets are noticed in Gr-10 min sample as it has more graphene concentrations of 0.5 wt.% compared to Gr5-10 min and Gr5-1 min samples of 0.05 wt.%. Further, graphene in these samples was added in the last phase of milling 1-10 minutes; hence it was able to maintain its structure. On the other hand, Gr5-20 hrs sample in which graphene was added at the beginning of milling does not show any graphene sheets in Figure 21 (e), as the brittle 2D structure was probably destroyed due to the long hours of milling.

To further asses the degree of crystallinity for graphene platelets, Raman spectroscopy analysis was done for all composite samples. Raman spectra for the two main peaks in carbon-based materials are G peak coming from the graphitic structure, and D peak originated from defective carbon, are shown in Figure 22 [51]. The range of Raman shifts values of the samples is shown in Table 4 and is in a similar range as other studies of graphene-based bismuth telluride composites [51, 52]. However, as shown in Figure 22, the intensity of these peaks was different in different samples. Hence, the intensity ratio of I_G/I_D, which gives an approximation of the degree of crystallinity for graphene platelets, was calculated, and the results are shown in Table 4. The I_G/I_D ratio for the as purchased graphene is 6.5. Comparing the ratio for the composite samples with as purchased graphene suggested the following. It was observed that milling graphene for the shortest time, in the sample where it was added at the last minute (e.g. Gr5-1 min), had a close value to as purchased graphene of 6.35; hence it preserved its crystallinity the most. Milling graphene for a longer time, in the samples where it was added at the last 10 minutes, Gr5-10 min and Gr-10 min, lowered the ratio a little. However, milling graphene for a longer time of 20 hours in the sample where it was added at the beginning, Gr5-20 hrs, had lowered the ratio greatly from 6.5 to 0.7, indicating that the crystallinity of graphene is almost destroyed at this stage, explaining why no graphene nanosheets were observed in the SEM image of this sample.

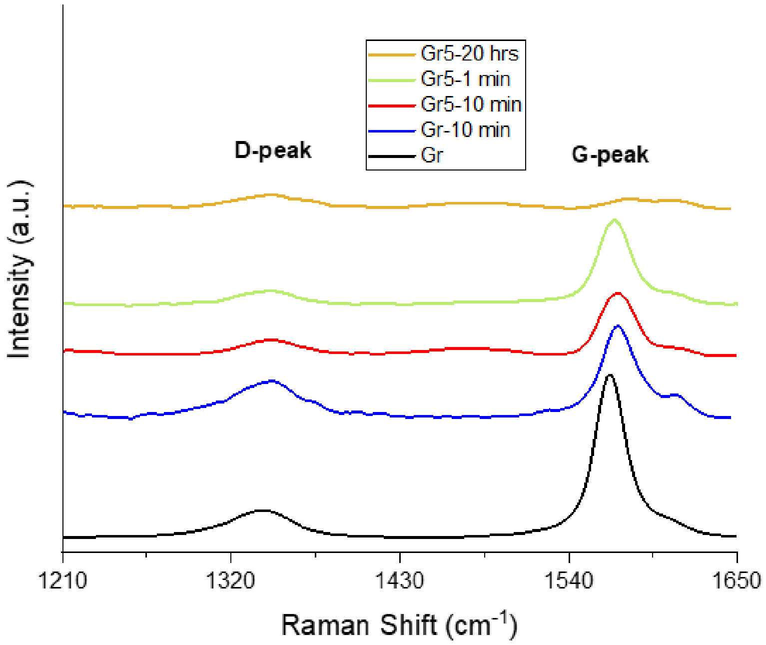

Figure 22: Raman Shift for Gr/$Bi_2Te_{2.7}Se_{0.3}$ composite samples.

Table 4

Raman Shift for Graphene in D and G Bands, and I_G/I_D Ratios of the Prepared Composites

Sample	Raman Shift (cm^{-1})		Intensity Ratio
	D	G	I_G/I_D
Gr	1338.6	1567.3	6.551
Gr-10 min	1346.0	1572.4	2.518
Gr5-10 min	1346.4	1572.4	4.413
Gr5-1 min	1342.4	1569.3	6.351
Gr5-20 hrs	1349.3	1594.6	0.732

TEM results represented as bright and dark field images for the as milled Gr5-10 min sample are shown in Figures 23 (a) and (b), respectively. The bright-field image shows equiaxial and randomly oriented grains. The dark field image was used to calculate the grain size and grain size distribution for more accurate results and is shown in Figure 23 (c). As presented, the average grain size is 19 ± 6 nm, which is slightly higher compared to the estimated grain size from XRD using Warren-Averbach model of 16.89 ± 1.3 nm, but still within the uncertainty range.

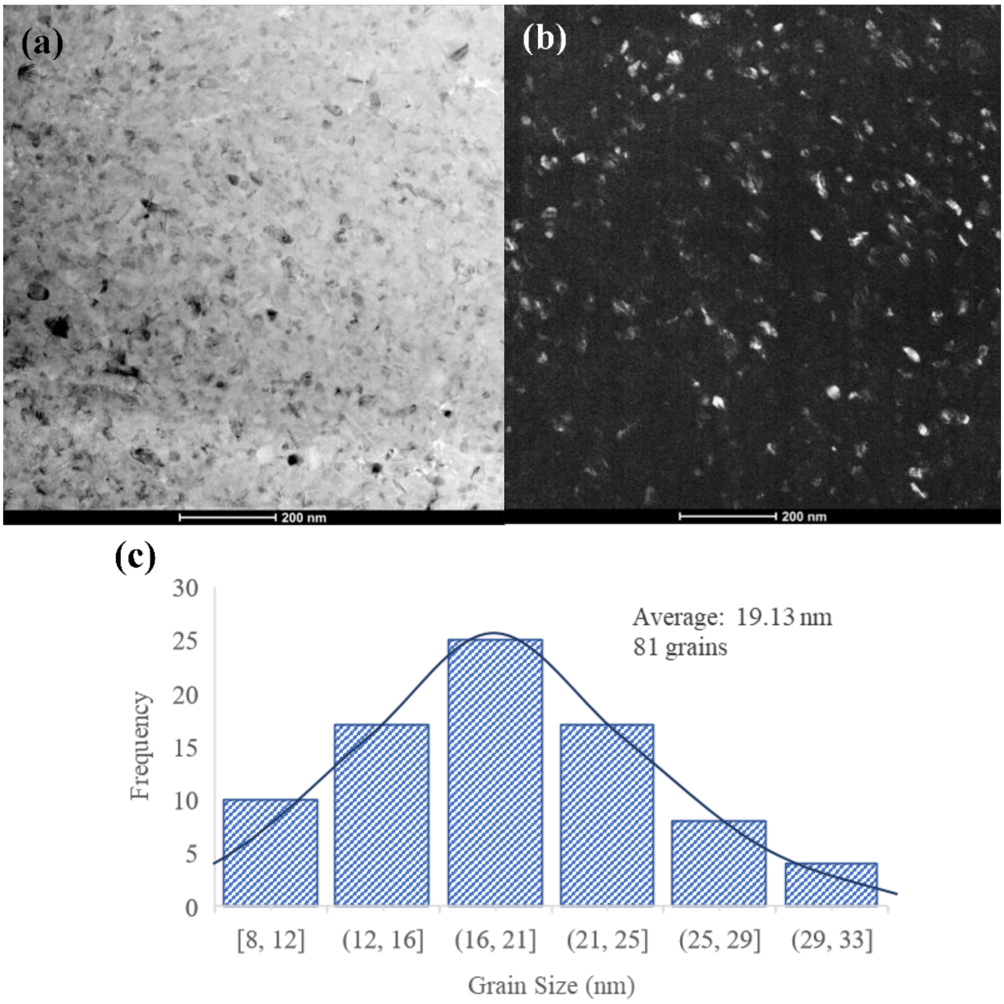

Figure 23: (a) bright field image, (b) dark field image, and (c) grain size distribution for Gr5-10 min sample.

The nonuniform distribution seen in the plot was noticed as well by Li et al. [16] who prepared graphene-based BiTe composite via solid-state reaction. The authors stated that the nonuniform distribution is due to the addition of graphene particles into the layered matrix. Moreover, Robinson [53] prepared doped n-type bismuth telluride using low energy ball milling. His results revealed a grain size of 17.7 nm after 72 hours of milling and 14.9 nm after 120 hours of milling. Due to the lower energy of the method, he applied, longer times were needed to reach a similar grain size as the sample under study. However, even after increasing the milling time by 35%, only less than 3 nm reduction was observed. In addition, Shin et al. [51] prepared reduced graphene oxide-based p-type bismuth telluride composite through the melt spinning process. The study reported that the grain size of the matrix reduces with the amount of graphene incorporated, which in return enhances the figure of merit value due to increased scattering events. Hence, graphene amount and ball milling hours are two important factors that affect the grain size of the material under study, and both can help in enhancing the final structure and thermoelectric properties.

Prepared Gr/$Bi_2Te_{2.7}Se_{0.3}$ Discs

Prior to conducting the thermoelectric measurements, XRD was done for all prepared discs, and the resulting plot is shown in Figure 24. Compared to the as milled power samples of the same composition, the peaks here are narrower and have lower intensities. This implies that the grain size of the samples is different. Also, there are more peaks showing for the discs. However, they all are related to the same reference of the pristine sample; thus, no contamination from the compaction process occurred. To further study the effect of the compaction process on the prepared discs, grain size calculations were done and are shown in Table 5. Again, Warren-Averbach model is a better fit with regressions greater than 0.9. The average grain size of the compacted bulk discs is 43.8 ± 4.7 nm, meaning a total increase of 160% compared to before compacting. This increase in grain size is expected and is mainly due to the high temperature used during the SPS process. This is because the grains at high temperatures tend to lower their internal energy by reducing the total area of grain boundaries by the recovery process.

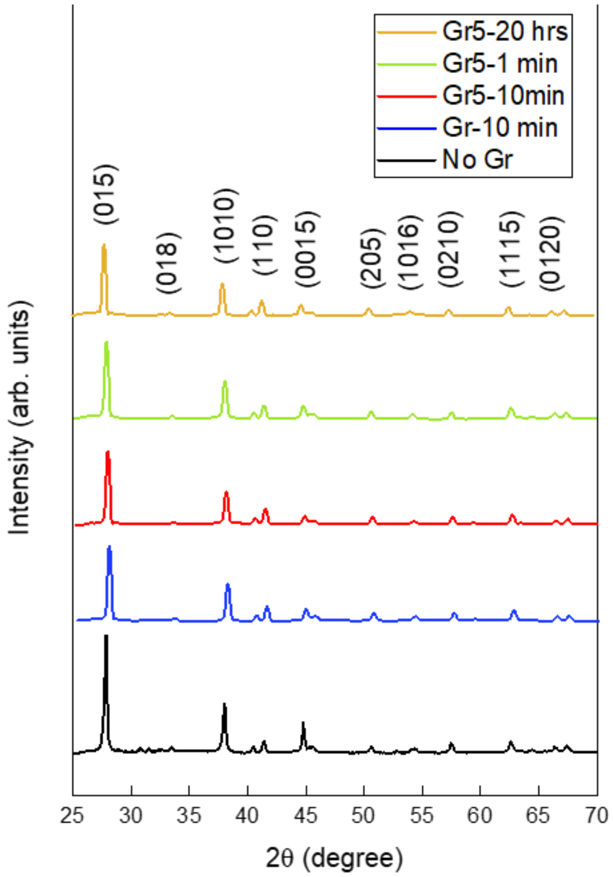

Figure 24: XRD for Gr/$Bi_2Te_{2.7}Se_{0.3}$ compacted discs.

Table 5

Grain Size of Gr/$Bi_2Te_{2.7}Se_{0.3}$ Compacted Discs

Sample Code	Grain Size (nm)			
	Warren-Averbach	R^2	Williamson-Hall	R^2
N-20 hrs	38.56	0.93	43.92	0.41
Gr-10 min	44.18	0.94	42.26	0.39
Gr5-10 min	45.16	0.96	42.54	0.51
Gr5-1 min	40.41	0.95	37.16	0.27
Gr5-20 hrs	50.73	0.91	55.08	0.46

In order to understand the effect of heat on the behavior of the milled samples, DSC was performed, and the results are shown in Figure 25. As the graph shows, all-composite samples, as well as the pristine one, have two main peaks. The first starts at an onset temperature around 375 ^{0}C, representing grain growth, while the second peak's onset starts around 415 ^{0}C and represents the melting point of matrix bismuth telluride [54]. This explains the increase of grain size as the compaction process was done at temperatures above grain growth peak, which is 580 ^{0}C. However, the grain size of the compacted discs is still in the nano-range and thus, improvements in the thermoelectric properties are expected.

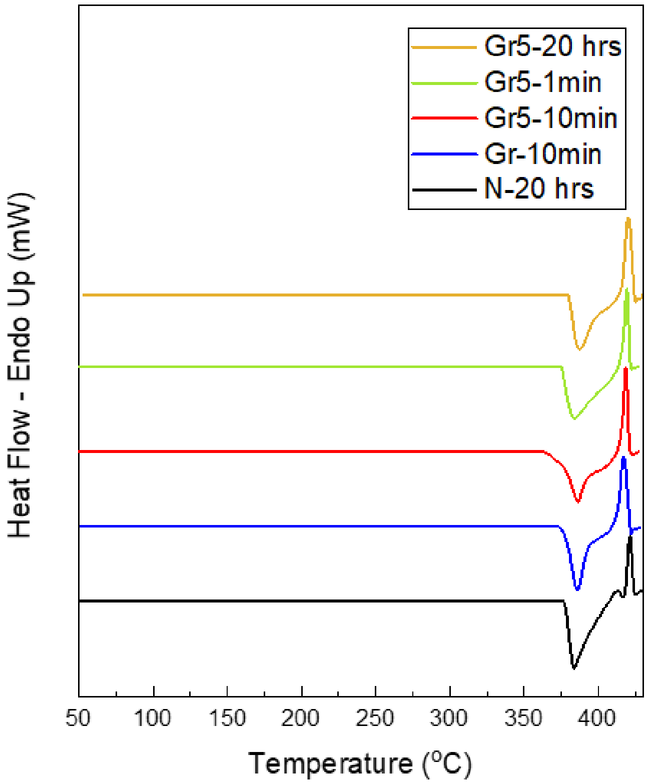

Figure 25: DSC results for Gr/$Bi_2Te_{2.7}Se_{0.3}$ composite samples.

Thermoelectric Properties of Gr/$Bi_2Te_{2.7}Se_{0.3}$ Discs

The results of the measurements for electrical conductivity, Seebeck coefficient, and thermal conductivity of the pristine sample, as well as the graphene-based bismuth telluride composites, are shown and explained next. From these measurements, the power factor and figure of merit values were also calculated and studied. All the results for the thermoelectric properties were studied starting from room temperature till 300 ºC since these alloys are used for near room-temperature applications [15].

Electrical Conductivity

Electrical conductivity trends for the compacted discs are shown in Figure 26. All samples showed a degenerate semiconductor behavior as their electrical conductivity decreases with temperature rise, which matches the trends of many graphene-based n-type bismuth telluride studies [1, 8, 30, 44]. The reduction of electrical conductivity with temperature rise is a result of the increased scattering process of electrons, which lowers their mobility at elevated temperatures [44]. This can be explained from equations (2) and (4) since an increase in the temperature, exponentially lowers the mobility at the interface, and hence contributes to lowering the total electrical conductivity. Moreover, the highest electrical conductivity values at room temperature are 1418 and 1265S/cm^3 for Gr5-1 min and Gr5-10 min samples, respectively. These are the samples with 0.05 wt.% graphene added in the last phase of mechanical milling. These samples showed higher electrical conductivity than the pristine one, hence enhancing the electrical properties of the composite. This result agrees with the outcomes of Ahmed et al. [8] who prepared graphene-based Bi_2Te_3 composites of concentrations of 0.5. 0.75 and 1.5 vol.%. The electrical conductivity for their composite samples was much higher than the base one. Ahmed et al. explained that graphene addition introduces a donor-like effect that contributed to enhancing the electrical conductivity of their composites. Hence, the addition of graphene in small amounts while preserving its structure increases the electrical conductivity of n-type doped bismuth telluride composites. On the other hand, the addition of graphene at the beginning or in higher concentrations in the composites led to a reduction in electrical conductivity values compared to pristine. Such reductions in electrical conductivities due to graphene addition were also noticed by Agarwal et al. [30] who prepared n-type bismuth telluride with 0.05 wt.% graphene monolayer composites. The variation in graphene presence effect on the electrical conductivity resulted from the tradeoff between the high conductivity of graphene filler used, the lowered carrier concentration resulted from the change in bandgap due to the interface introduced, and because of the increased aggregation and carrier scattering at interfacial boundaries [55]. Hence, depending on the amount and stability of graphene during milling, electrical conductivity values can be tuned.

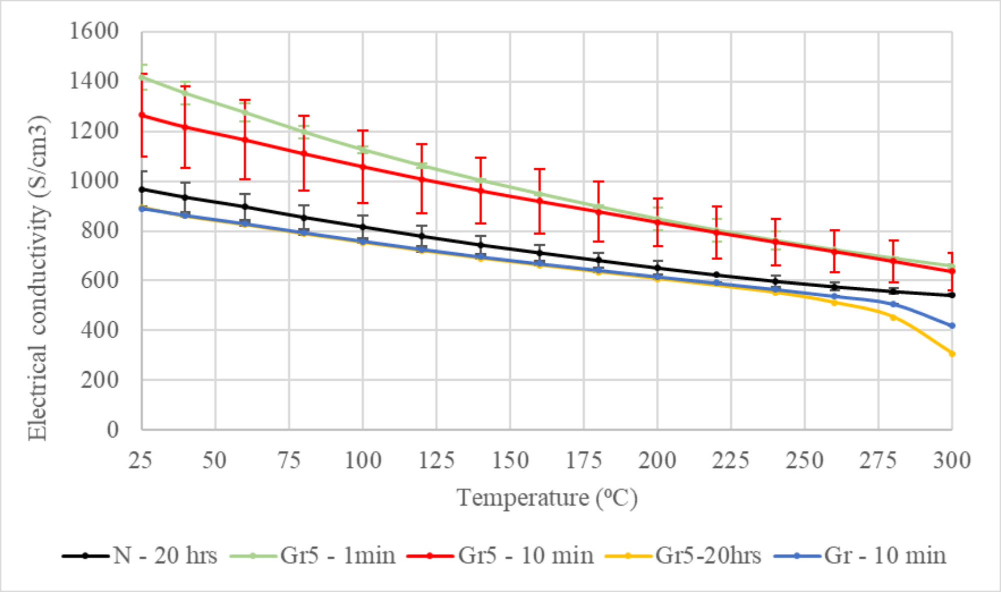

Figure 26: Electrical conductivity trends for Gr/$Bi_2Te_{2.7}Se_{0.3}$ samples.

Seebeck Coefficient

Seebeck coefficient trends versus temperature for the composite samples are shown in Figure 27. The negative values of Seebeck imply that all samples are n-type, where electrons are the main charge carriers. Taking absolute values, the optimum temperature is 160 ^{0}C, and the maximum value of Seebeck reached is -155 µV/K for Gr5-20 hrs sample, hence a total enhancement of 5%. All other composite samples showed a reduction in Seebeck coefficient values compared to pristine. The main difference between the improved and unimproved samples is the phase in which graphene was added to the mill. Apparently, adding graphene at the beginning of the mill leads to an increase in the Seebeck coefficient. Similar high increases in the Seebeck coefficient were noticed by Ahmad et al. [8] who prepared the Gr/Bi2Te3 composite through ultra-sonification and ball milling. On the other hand, there are studies of graphene-based n-type bismuth telluride, which showed reductions in the Seebeck coefficient for the composites compared to pristine. However, these were prepared using other mixing techniques like solid-state reaction [16], the reflexing method [1], and hydrothermal synthesis [44]. Moreover, at room temperature, the highest Seebeck value of -128 μV/K is for Gr5-20 hrs sample. Followed by -120 μV/K for N-20 hrs, then -118 μV/K for Gr-10 min, -117 μV/K for Gr5-10 min and finally -109 μV/K for Gr5-1 min sample. The opposite order of enhancing and diminishing for the composite samples in the previous two parameters (electrical conductivity and Seebeck coefficient) is a result of their different proportionality to the charge carrier concentration [30].

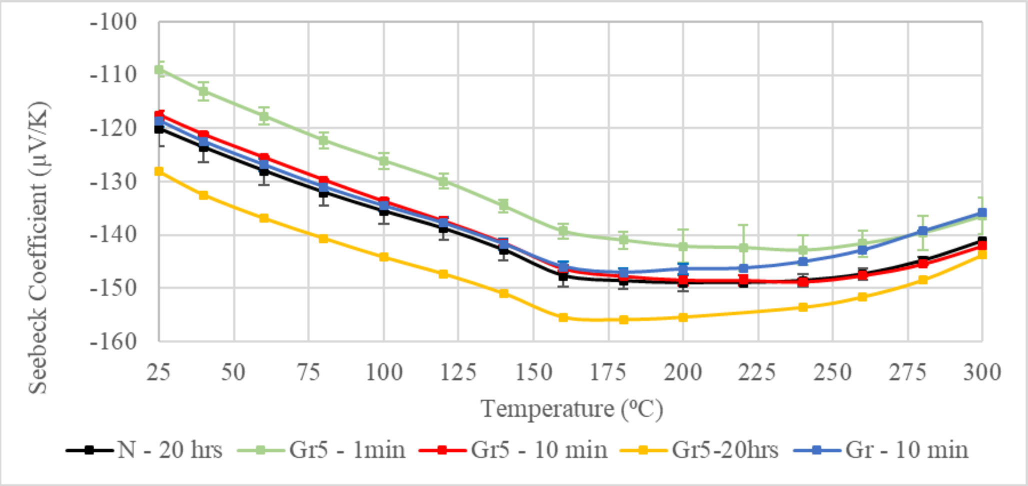

Figure 27: Seebeck coefficient trends for Gr/$Bi_2Te_{2.7}Se_{0.3}$ samples.

Power Factor

Power factor ($S^2\sigma$) is a representation of the combined effect of the previous two thermoelectric properties, and its trend is shown in Figure 28. In general, samples with 0.05 wt.% graphene showed higher values, while 0.5 wt.% sample showed lower value, compare to pristine $Bi_2Te_{2.7}Se_{0.3}$ sample. The optimum temperature is 160 ºC, and the best sample is Gr5-10 min. Further, at room temperature, the pristine sample had a power factor of 1.4 mW/mK^2, which is slightly lower compared to values obtained by other studies who prepared similar n-type composition of pristine bismuth telluride through ball milling such as Kim et al. [7] who got a power factor value of 1.63 mW/mK^2 and Nozariasbmarz et al. [56] who obtained 1.87 mW/mK^2. The addition of graphene, in the case under study, improved the power factor value to 1.75 mW/mK^2 for the optimum Gr5-10 min sample at 25 ºC. The optimum two samples, which are with lower graphene concentration added during the last phase of mechanical milling, were used for the renaming thermoelectric properties investigation.

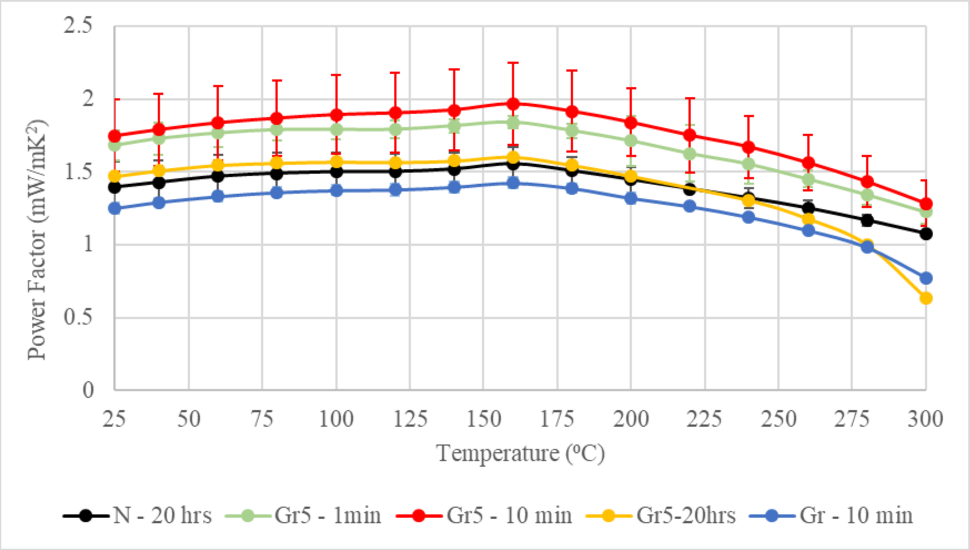

Figure 28: Power factor trends for Gr/$Bi_2Te_{2.7}Se_{0.3}$ samples.

Thermal Conductivity

Thermal conductivity trends for the two optimized samples of highest power factors, as well as the pristine sample, are shown in Figure 29. According to the obtained results, graphene addition increased the thermal conductivity of the composites. This does not match most of the studies who used graphene as a filler for n-type undoped bismuth telluride and reasoned the reduction by the introduction of new scattering events due to filler addition [1, 8, 30, 44]. Hence, to further understand the effect of the total thermal conductivity, the electronic and lattice parts were calculated using equations (6) and (7), and their plots are shown in Figures 30 and 31. As shown, the lattice part of the total thermal conductivity reveals lower values for graphene-based composite samples, matching the studies mentioned previously. On the other hand, the electronic part of the total thermal conductivity had an opposite effect on the composite samples. This effect, as equation (7) explains, is mainly due to the extremely high electrical conductivity for these two samples, which are 30-45% higher than the pristine one. The effect of the electronic part was more dominant, hence leading to an undesirable rise in the total thermal conductivity.

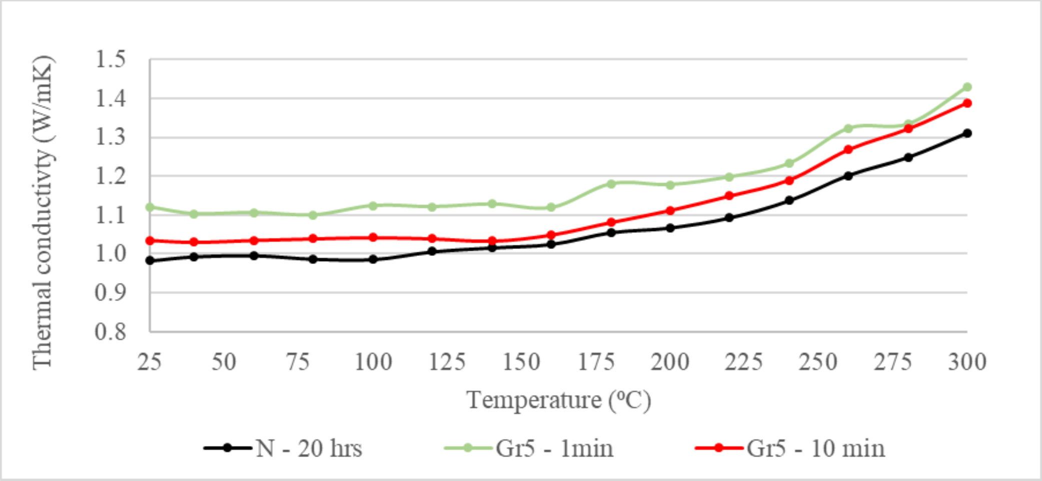

Figure 29: Thermal conductivity trends for pristine and optimized samples.

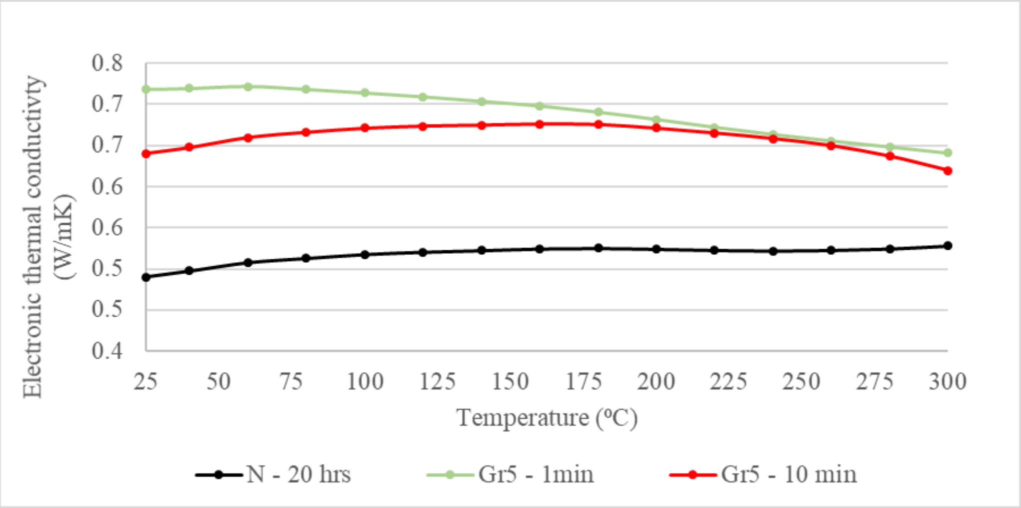

Figure 30: Electronic thermal conductivity trends for pristine and optimized samples.

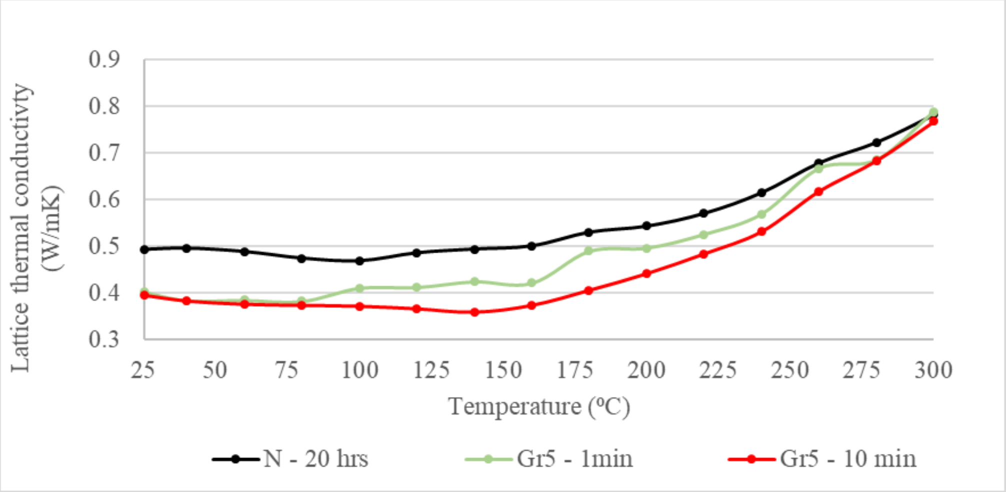

Figure 31: Lattice thermal conductivity trends for pristine and optimized samples.

The Figure of Merit

The total effect of all previous parameters, represented through figure-of-merit, is shown in Figure 32. Generally, the improvements in the power factor had more effect on the ZT than the undesirable increment of the total thermal conductivities. Hence, enhancements in ZT were observed for graphene composites. Figure-of-merit trends show the highest ZT for Gr5-10 min sample, followed by Gr5-1 min sample, then the pristine one. At room temperature, the ZT improved due to graphene addition by 19% from 0.42 to 0.5 for the optimum sample, whereas at the optimum temperature of 160 ºC, ZT had a total improvement of 23% reaching a value of 0.81, for the same sample. The other samples also exhibit an enhancement of 7-8% compared to the pristine bismuth telluride.

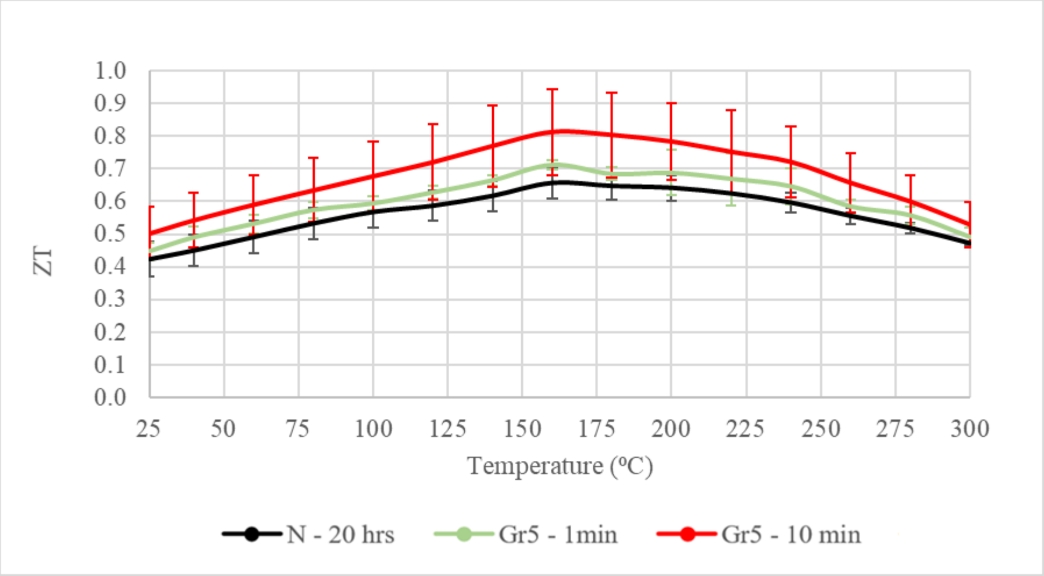

Figure 32: ZT trends for pristine and optimized Gr/$Bi_2Te_{2.7}Se_{0.3}$ samples.

Comparing these results to published work for n-type undoped Gr/Bi_2Te_3 samples reveals good overall improvements, as seen in Figure 33. Through ultra-sonification and ball milling, Ahmed et al. [8] reached a maximum ZT value of 0.55 at 227 ºC and 0.29 at room temperature with improvements of 588% and 190%, respectively. Regardless of the very high percentages, the ZT is lower than the sample under study since their pristine suffered from a very low figure-of-merit. Liang et al. [44] used hydrothermal synthesis and obtained an optimum ZT value of 0.21 at 200 ºC for a composite containing 0.2 vol.% graphene nanosheets. Moreover, Ju and Kim [45] prepared Gr/Bi_2Te_3 composite with several graphene concentrations but with two different bismuth telluride matrixes, powder, and nanowires. The composites were prepared via wet-chemical synthesis and studied at room temperature. Only some of the filler concentrations, the low ones, showed improvements in ZT. Adding reduced graphene oxide filler to powder Bi_2Te_3 matrix enhanced the optimum concentration of 1 wt.% from 0.24 till 0.3, whereas using nanowire Bi_2Te_3 as a matrix improved ZT from 0.31 to 0.4. Nevertheless, these values are lower compared to the doped bismuth telluride composites under study. Kumar et al. [1] also used reduced graphene oxide to prepare n-type composite via the reflexing method and reached a maximum ZT of 0.35 at 70 ^oC. On the other hand, Agrawal et al. [50] prepared 0.05 wt.% graphene monolayer based Bi_2Te_3 by simply mixing the purchased powders using agate mortar and pestle. The research group obtained a high ZT value for the composite of 0.92 at 130 ^oC compared to 0.68 for the pristine. This high increase was due to improving the thermoelectric properties of the sample through enhancing the Seebeck coefficient rather than electrical conductivity. Thus, this study is the first that examines the effect of graphene addition into **doped** n-type $Bi_2Te_{2.7}Se_{0.3}$, and the prepared samples had higher ZT than most of the published data.

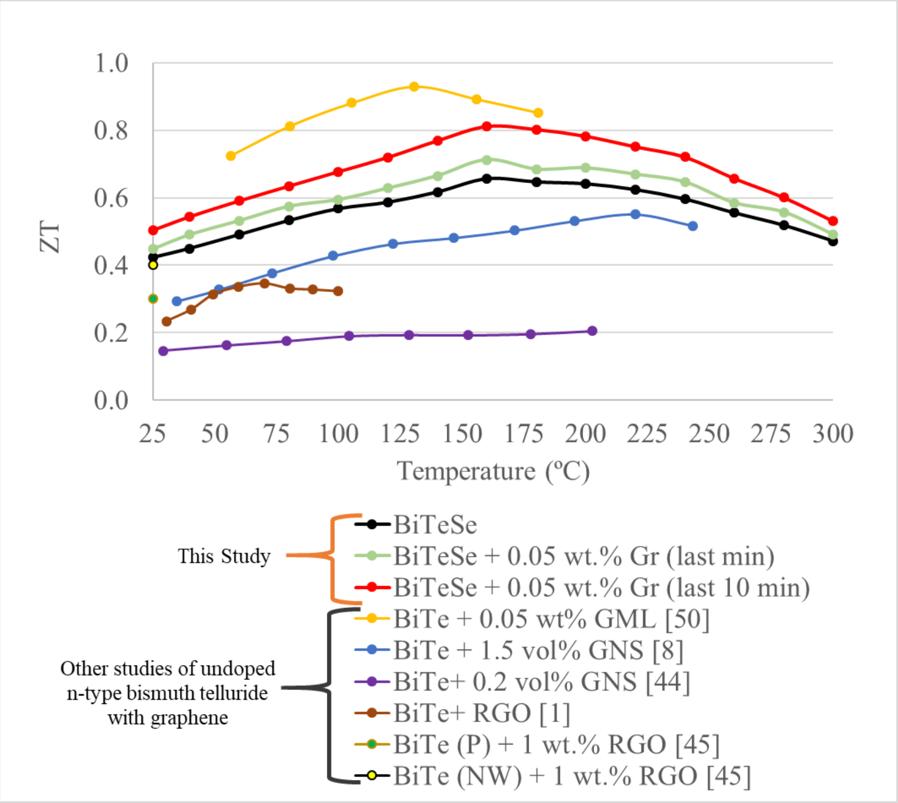

Figure 33: Comparing obtained ZT with other studies, where GML is graphene monolayer, GNS is graphene nanosheet, RGO is reduced graphene oxide, P is powder and NW is nanowire.

CHAPTER 5: CONCLUSION

In conclusion, graphene-based n-type bismuth telluride (G/$Bi_2Te_{2.7}Se_{0.3}$) nanocomposite was successfully prepared through ball milling technique. Powders were compacted using SPS and their thermoelectric properties were measured. The final thesis remarks are:

- The optimum milling time to produce nanostructured n-type material is 20 hours.
- The prepared as milled powders had an average grain size of 17 ± 1 nm and after SPS process, the average grain size increased to 44 ± 5 nm.
- Hardness values for the graphene composites showed higher values for 0.5 wt.% graphene concentration, and lower values for 0.05 wt.% samples, compared to pristine sample, hence showing the ability of graphene amount on tuning the hardness of the samples.
- The micro Raman analysis showed that mechanical milling of graphene at short milling times results in maintaining the integrity of graphene nanostructure in the composites.
- Electrical conductivity trends showed the best results for samples with 0.05 wt.% graphene added in the last phase of mechanical milling, with up to 45% enhancements.
- Seebeck coefficient values were enhanced only for the sample where graphene was added at the beginning.
- The power factor parameter showed that the optimum samples are the ones with 0.05 wt.% graphene added in the last phase of mechanical milling.
- High graphene percentage resulted in lower power factor compared to pristine.

- The undesirable increase in the total thermal conductivity resulted from the dominant effect of the electronic part of the parameter due to the high electrical conductivities of the samples.
- Regardless of the undesirable increase in thermal conductivity, the final figure of merit values showed enhancements due to graphene addition.
- The addition of 0.05 wt.% graphene increased the ZT by 19% at RT and by 23% at 160 ºC over that of the pristine sample.
- Both the nanostructuring and the presence of graphene nanofiller could be the reason of the ZT enhancement.
- Even though the final ZT was less than 1, high improvements were achieved compared to most published data.
- Compacting the samples at temperatures lower than 375 ºC is expected to show better results and higher ZT values.
- A full investigation of the sample with the highest ZT value in order to understand the structural reasons (such as using HR-TEM and STEM) would enable to further tailor the thermoelectric properties.
- Even though the SPS is a widespread technique to consolidate such materials, recent results indicate the presence of micro and sub-micro cracks in the compacted discs, which deteriorate the thermoelectric properties. Therefore, the usage of another consolidation (such as Hot Isostatic Pressing) could eliminate the influence of these defects and show better enhancements.

REFERENCES

1. Kumar S, Singh S, Dhawan PK, Yadav RR, Khare N. Effect of graphene nanofillers on the enhanced thermoelectric properties of Bi2Te3 nanosheets: elucidating the role of interface in de-coupling the electrical and thermal characteristics. 2018.
2. Ju H, Kim M, Kim J. Preparation of graphene sheets into one-dimensionally nanostructured bulk bismuth telluride for enhancing thermoelectric power factor. 2016. p. 3427-34.
3. Zhang Y, Ma H, Sun B, Liu B, Liu H, Kong L, et al. Thermoelectric performance of graphene composited BiSbTe bulks by high pressure synthesis. Journal of Alloys and Compounds. 2017;715:344-8.
4. Kanatzidis MG. Nanostructured Thermoelectrics: The New Paradigm? 2010. p. 648-59.
5. Xie W, Tang X, Yan Y, Zhang Q, Tritt TM. High thermoelectric performance BiSbTe alloy with unique low-dimensional structure. Journal of Applied Physics. 2009;105(11):113713-21.
6. Fan S, Zhao J, Guo J, Yan Q, Ma J, Hng HH. p-type Bi0.4Sb1.6Te3 nanocomposites with enhanced figure of merit. 2010.
7. Kim KT, Lim TS, Ha GH. IMPROVEMENT IN THERMOELECTRIC PROPERTIES OF N-TYPE BISMUTH TELLURIDE NANOPOWDERS BY HYDROGEN REDUCTION TREATMENT. 2011. p. 196-9.
8. Ahmad K, Wan C, Al-Eshaikh MA, Kadachi AN. Full Length Article: Enhanced thermoelectric performance of Bi2Te3 based graphene nanocomposites. Applied Surface Science. 2018.
9. Beibei L, Zijun S, Minghui W, Lianjun W, Wan J. Fabrication and Thermoelectric

Properties of Graphene/Bi2Te3 Composite Materials. 2013:1-5.

10. Mamur H, Bhuiyan MRA, Korkmaz F, Nil M. A review on bismuth telluride (Bi2Te3) nanostructure for thermoelectric applications. Renewable and Sustainable Energy Reviews. 2018;82:4159-69.
11. Rahman A, Umar A, Chen X, Salleh M, Oyama M. Enhanced thermoelectric properties of bismuth telluride-organic hybrid films via graphene doping. Applied Physics A: Materials Science & Processing. 2016;122(2):1-8.
12. Ouyang Y, Guo J. A theoretical study on thermoelectric properties of graphene nanoribbons. 2009.
13. Li C, Qin X, Li Y, Li D, Zhang J, Guo H, et al. Simultaneous increase in conductivity and phonon scattering in a graphene nanosheets/(Bi2Te3)0.2(Sb2Te3)0.8 thermoelectric nanocomposite. Journal of Alloys and Compounds. 2016;661:389-95.
14. Peng J, Gao W, Gupta BK, Liu Z, Romero-Aburto R, Ge L, et al. Graphene Quantum Dots Derived from Carbon Fibers. 2012. p. 844-9.
15. Neeli G, Behara D, Kumar M. State of the Art Review on Thermoelectric Materials. International Journal of Science and Research. 2015.
16. Li AH, Shahbazi M, Zhou SH, Wang GX, Zhang C, Jood P, et al. Electronic structure and thermoelectric properties of Bi2Te3 crystals and graphene-doped Bi2Te3. Thin Solid Films. 2010;518(Supplement):e57-e60.
17. An H, Pusko M, Chun D, Park S, Moon J. In-situ synthesis of flexible hybrid composite films for improved thermoelectric performance. Chemical Engineering Journal. 2019;357:547-58.
18. Witting IT, Ricci F, Chasapis TC, Hautier G, Snyder GJ. The Thermoelectric Properties of -Type Bismuth Telluride: Bismuth Selenide Alloys. Research.

2020;2020:15.

19. Takashiri M, Takiishi M, Tanaka S, Miyazaki K, Tsukamoto H. Thermoelectric properties of n-type nanocrystalline bismuth-telluride-based thin films deposited by flash evaporation. Journal of Applied Physics. 2007;101(7):074301-5.
20. Fan S, Zhao J, Yan Q, Ma J, Hng HH. Influence of Nanoinclusions on Thermoelectric Properties of n-Type Bi2Te3 Nanocomposites. 2011. p. 1018-23.
21. Suryanarayana C. Mechanical Alloying And Milling. Bosa Roca, United States: Taylor & Francis Inc; 2004.
22. Suh D, Lee S, Mun H, Park S-H, Lee KH, Wng Kim S, et al. Rapid communication: Enhanced thermoelectric performance of Bi0.5Sb1.5Te3-expanded graphene composites by simultaneous modulation of electronic and thermal carrier transport. 2015;13:67-76.
23. Lognoné Q, Gascoin F. On the effect of carbon nanotubes on the thermoelectric properties of n-Bi2Te2.4Se0.6 made by mechanical alloying. Journal of Alloys & Compounds. 2015;635:107-11.
24. Kim KT, Choi SY, Shin EH, Moon KS, Koo HY, Lee G-G, et al. The influence of CNTs on the thermoelectric properties of a CNT/Bi2Te3 composite. Carbon. 2013;52:541-9.
25. Orton J. CHAPTER 6 - Quantum Theory and Quantum Practice: The Nanostructure Revolution. In: Orton J, editor. Semiconductors and the Information Revolution. Amsterdam: Academic Press; 2009. p. 163-92.
26. Zhang Q, Ai X, Wang L, Chang Y, Luo W, Jiang W, et al. Improved Thermoelectric Performance of Silver Nanoparticles-Dispersed Bi2Te3 Composites Deriving from Hierarchical Two-Phased Heterostructure. Advanced Functional Materials. 2015;25(6):966-76.

27. Li J-F, Liu J. Effect of nano-SiC dispersion on thermoelectric properties of Bi2Te3 polycrystals. 2006. p. 3768-73.

28. Jiang Q, Yang J, Xin J, Zhou Z, Zhang D, Yan H. Carriers concentration tailoring and phonon scattering from n-type zinc oxide (ZnO) nanoinclusion in p- and n-type bismuth telluride (Bi2Te3): Leading to ultra low thermal conductivity and excellent thermoelectric properties. Journal of Alloys and Compounds. 2017;694:864-8.

29. Liu D-W, Li J-F, Chen C, Zhang B-P. Effects of SiC Nanodispersion on the Thermoelectric Properties of p-Type and n-Type Bi2Te3-Based Alloys. 2011. p. 992-8.

30. Agarwal K, Kaushik V, Varandani D, Dhar A, Mehta BR. Nanoscale thermoelectric properties of Bi2Te3 – Graphene nanocomposites: Conducting atomic force, scanning thermal and kelvin probe microscopy studies. Journal of Alloys & Compounds. 2016;681:394-401.

31. Kulbachinskiia V, Kytina V, Blankb V, Bugab S, Popov M. Thermoelectric Properties of Bismuth Telluride Nanocomposites with Fullerene. Semiconductors. 2015;45:1194-8.

32. Trawinski B, Bochentyn B, Gostkowska N, Lapinski M, Miruszewski T, Kusz B. Structure and thermoelectric properties of bismuth telluride-Carbon composites. 2018. p. 10-7.

33. Li Y, Zhao Q, Wang Y-g, Bi K. Synthesis and characterization of Bi2Te3/polyaniline composites. Materials Science in Semiconductor Processing. 2011;14(3/4):219-22.

34. Tae Kim K, Seong Eom Y, Son I. Fabrication Process and Thermoelectric Properties of CNT/Bi2(Se,Te)3 Composites. Journal of Nanomaterials.

2014;2015.

35. Kumar S, Chaudhary D, Dhawan PK, Yadav RR, Khare N. Bi2Te3-MWCNT nanocomposite: An efficient thermoelectric material. 2017. p. 14976-82.

36. Bark H, Kim J-S, Kim H, Yim J-H, Lee H. Effect of multiwalled carbon nanotubes on the thermoelectric properties of a bismuth telluride matrix. Current Applied Physics. 2013;13(Supplement 2):S111-S4.

37. Zhang Y, Wang XL, Yeoh WK, Zheng RK, Zhang C. Electrical and thermoelectric properties of single-wall carbon nanotube doped Bi2Te3. 2012.

38. Park D-H, Kim M-Y, Oh T-S. Thermoelectric energy-conversion characteristics of n-type Bi2(Te,Se)3 nanocomposites processed with carbon nanotube dispersion. Current Applied Physics. 2011;11(4):S41-S5.

39. Ao W, Wang L, Li J, Pan F, Wu C. Synthesis and Characterization of Polythiophene/BiTe Nanocomposite Thermoelectric Material. Journal of Electronic Materials. 2011;40(9):2027.

40. Anno Y, Takei K, Akita S, Arie T. Enhancing the Thermoelectric Device Performance of Graphene Using Isotopes and Isotopic Heterojunctions. 2015.

41. Yang G, Li L, Lee WB, Ng MC. Structure of graphene and its disorders: a review. Science and Technology of Advanced Materials. 2018;19(1):613-48.

42. Chang P-H, Bahramy MS, Nagaosa N, Nikolic BK. Giant Thermoelectric Effect in Graphene-Based Topological Insulators with Heavy Adatoms and Nanopores. 2014. p. 3779-84.

43. Dragoman D, Dragoman M. Giant thermoelectric effect in graphene. 2007.

44. Liang B, Song Z, Wang M, Wang L, Jiang W. Fabrication and Thermoelectric Properties of Graphene/Bi2Te3 Composite Materials. 2013.

45. Ju H, Kim J. Preparation and structure dependent thermoelectric properties of

nanostructured bulk bismuth telluride with graphene. Journal of Alloys and Compounds. 2016;664:639-47.

46. Youssef KM, Scattergood RO, Murty KL, Koch CC. Nanocrystalline Al–Mg alloy with ultrahigh strength and good ductility. Scripta Materialia. 2006;54(2):251-6.
47. Khorsand Zak A, Abd. Majid WH, Abrishami ME, Yousefi R. X-ray analysis of ZnO nanoparticles by Williamson–Hall and size–strain plot methods. Solid State Sciences. 2011;13(1):251-6.
48. Britannica TEoE. Vickers Hardness. Encyclopaedia Britannica: Encyclopædia Britannica; 2018.
49. T. Degen MS, E. Bron, U. König, G. Nénert; . The HighScore suite. Powder Diffraction. 2014;29(S 2): S 13-S 8.
50. Agrawal S, Rai MK. Performance analysis of multi walled carbon nanotube (MWCNT) bundle as VLSI interconnects. 2015.
51. Shin WH, Ahn K, Jeong M, Yoon JS, Song JM, Lee S, et al. Enhanced thermoelectric performance of reduced graphene oxide incorporated bismuth-antimony-telluride by lattice thermal conductivity reduction. Journal of Alloys and Compounds. 2017;718:342-8.
52. Ju H, Kim J. The effect of temperature on thermoelectric properties of n-type Bi2Te3 nanowire/graphene layer-by-layer hybrid composites. 2015.
53. Robinson CA, editor Preparation of bismuth telluride based thermoelectric nanomaterials via low-energy ball milling and their property characterizations2015.
54. Schick C. 2.31 - Calorimetry. In: Matyjaszewski K, Möller M, editors. Polymer Science: A Comprehensive Reference. Amsterdam: Elsevier; 2012. p. 793-823.
55. Kim EB, Dharmaiah P, Shin D, Lee K-H, Hong S-J. Enhanced thermoelectric

performance through carrier scattering at spherical nanoparticles in $Bi_{0.5}Sb_{1.5}Te_3/Ta_2O_5$ composites. Journal of Alloys & Compounds. 2017;703:614-23.

56. Nozariasbmarz A, Krasinski SJ, Vashaee D. N-Type Bismuth Telluride Nanocomposite Materials Optimization for Thermoelectric Generators in Wearable Applications. Materials. 2019;12(9).